Saharan Dust Impact on Radiative Heating Rate Errors Inherent in Reanalysis Data in the African Easterly Wave Development Region

Ruby W. Burgess

A Thesis submitted in partial fulfillment of

the requirements for the degree of

Master of Science

(Atmospheric and Oceanic Sciences)

at the

University of Wisconsin-Madison

July 2024

Thesis Declaration and Approval

I, Ruby W. Burgess, declare that this Thesis titled 'Saharan Dust Impact on Radiative Heating Rate Errors Inherent in Reanalysis Data in the African Easterly Wave Development Region' and the work presented in it are my own.

Ruby W. Burgess		
Author	Signature	Date

I hereby approve and recommend for acceptance this work in partial fulfillment of the requirements for the degree of Master of Science:

Mayra I. Oyola-Merced		
Committee Chair	Signature	Date

Tristan S. L'Ecuyer		
Faculty Member	Signature	Date

Angela K. Rowe		
Faculty Member	Signature	Date

Daniel J. Vimont		
Faculty Member	Signature	Date

Abstract

Saharan Dust Impact on Radiative Heating Rate Errors Inherent in Reanalysis Data in the African Easterly Wave Development Region

by Ruby W. Burgess

Saharan dust outbreaks strongly impact the atmosphere's energy balance, as their radiative effects can alter atmospheric heating rates by several degrees per day. However, numerical weather prediction models often struggle to accurately represent aerosol vertical distribution, leading to forecast errors driven by biases in heating rates. Utilizing a four-stream radiative transfer model and data from reanalysis as well as dropsonde profiles and lidar observations from NASA's CPEX-CV field campaign, this study examines the impact of Saharan dust on atmospheric heating rates over the North Atlantic Ocean, with a specific focus on the African Easterly Wave (AEW) development region. The performance of two reanalyses, MERRA-2 and CAMS, is evaluated, and results reveal notable differences in aerosol-induced shortwave heating of over 1.5 K/day between reanalysis and field observations. These findings underline the persistent challenges in accurately representing aerosol effects in the atmosphere, even after the assimilation of observational data. A case study of three developing AEWs during the CPEX-CV field campaign highlights a difference in aerosol-induced heating on the order of 1 to 2 K/day between two AEWs developing into major hurricanes and one developing into a short-lived tropical storm, raising the question of the role of dust-induced heating in AEW development.

Acknowledgements

I would like to thank my advisor, Mayra Oyola-Merced, for having taken me on as a graduate student and for your continued support these past two years. Through your mentorship, I have grown as a researcher, coder, and scientist. To you and my committee, Tristan L'Ecuyer, Angela Rowe, and Dan Vimont, I am extremely grateful for your guidance and feedback during the process of completing my master's research project and thesis. I would also like to thank the CPEX-CV team for their support and feedback on this project.

To my mom, Sandrine, my dad, Gregory, and siblings, Emma, Adele, and Zachary: Thank you for your support and faith in my dreams even though they have taken me halfway across the world. Your support from afar was not only helpful, but essential. To my friends that I left back home, the ones I made in the last six years, and the ones that have made Wisconsin feel a little more like home: thank you so much for being there for me every step of the way. I couldn't have done this without you.

Finally, to my teachers and professors, from preschool to present-day: your collective influence has been instrumental in my journey. From fostering my love for science to challenging me academically and encouraging me to pursue my passions, each of you has contributed to my growth in many ways. I am deeply grateful for the lessons you have taught me - thank you for being a vital part of my educational journey.

Contents

List of Figures

List of Tables

Abbreviations

AEW	**A**frican **E**asterly **W**ave
AOD	**A**erosol **O**ptical **D**epth
AVAPS	**A**dvanced **V**ertical **A**tmospheric **P**rofiling **S**ystem
CALIPSO	**C**loud-**A**erosol **L**idar and **I**nfrared **P**athfinder **S**atellite **O**bservations
CAMS	**C**opernicus **A**tmosphere **M**onitoring **S**ervice
CCN	**C**loud **C**ondensation **N**ucleus
CPEX-CV	**C**onvective **P**rocesses **Ex**periment – **C**abo **V**erde
EarthCARE	**Earth C**loud, **A**erosol and **R**adiation **E**xplorer
FLG	**F**u-**L**iou-**G**u
GOCART	**Go**ddard **C**hemistry **A**erosol **R**adiation and **T**ransport
GPM	**G**lobal **P**recipitation **M**easurement
HALO	**H**igh **A**ltitude **L**idar **O**bservatory
IR	Infrared
ITCZ	**I**nter-**T**ropical **C**onvergence **Z**one
LW	Longwave
MERRA-2	**M**odern-**E**ra **R**etrospective Analysis for **R**esearch and **A**pplications, Version **2**
NASA	**N**ational **A**eronautics and **S**pace **A**dministration
NWP	**N**umerical **W**eather **P**rediction
OPAC	**O**ptical **P**roperties of **A**erosols and **C**louds
RTM	**R**adiative **T**ransfer **M**odel
SAL	**S**aharan **A**ir **L**ayer

SW	Shortwave
TC	**T**ropical **C**yclone

Physical Constants

Specific Heat Capacity of Air at Constant Pressure $C_p = 1005 \text{ J kg}^{-1} \text{ K}^{-1}$

Symbols

F_i	radiative flux	W m^{-2}
k_e	mass extinction coefficient	m^2 kg^{-1}
p	pressure	hPa
Q_{ext}	extinction efficiency	
q	specific humidity	kg kg^{-1}
R_{DU}	dust mass mixing ratio	kg kg^{-1}
R_d	gas constant for dry air	J kg^{-1} K^{-1}
r	particle radius	m
T	temperature	K
T_v	virtual temperature	K
ρ_{air}	air density	kg m^{-3}
ρ_p	particle density	kg m^{-3}
τ_i	band average flux transmittance	

Chapter 1

Introduction

1.1 Aerosol Properties

1.1.1 Aerosol Background

Aerosol particles, or aerosols, are particles that are small enough to remain suspended in the atmosphere for a significant amount of time, from several hours to weeks or more. They are defined as particles in the solid or liquid phase, dispersed in a gaseous medium such as the atmosphere. These particles typically range from sizes on the order of 10^{-3} µm to 100 µm (Prospero et al., 1983), and examples of aerosols include sea salt, mineral dust, black carbon, and volcanic ash. Aerosols are either classified as fine mode, which comprises Aitken particles of radius less than 0.2 µm and large (or accumulation-mode) particles of radius 0.2 to 2 µm, or as coarse mode, which comprises giant particles of

radius greater than 2 µm and ultragiant particles of radius greater than 20 µm (Prospero et al., 1983).

1.1.2 Atmospheric Impact of Aerosols

Aerosols directly affect the Earth's radiative balance by absorbing or scattering solar radiation, depending on their physical and optical properties. They also indirectly affect the Earth's radiative balance by impacting cloud microphysics and precipitation (e.g., by acting as cloud condensation nuclei (CCN) or ice condensation nuclei (ICN)) (Bauer and Menon, 2012, Ramanathan et al., 2001) as well as by altering atmospheric energy balances and stability by heating or cooling the atmosphere which alters weather systems (Grogan et al., 2016). Aerosol concentration, composition, hygroscopicity, size distribution, vertical distribution and mixing state act to influence heating rates in the Earth's atmosphere, in turn affecting the development of weather systems. Size distribution as well as composition determines single scatter albedo, which describes the relative amounts of scattering and absorption of an aerosol. Aerosol concentration affects the amount of scattering and absorption of solar radiation, directly impacting the total amount of atmospheric heating or cooling. Vertical distribution determines the atmospheric heating profile, which in turn can impact energy balance and weather dynamics. Understanding these properties is essential to improving numerical weather prediction (NWP) models and the accuracy of reanalysis data outputs, as well as strengthening our understanding of the impact of aerosols on weather systems.

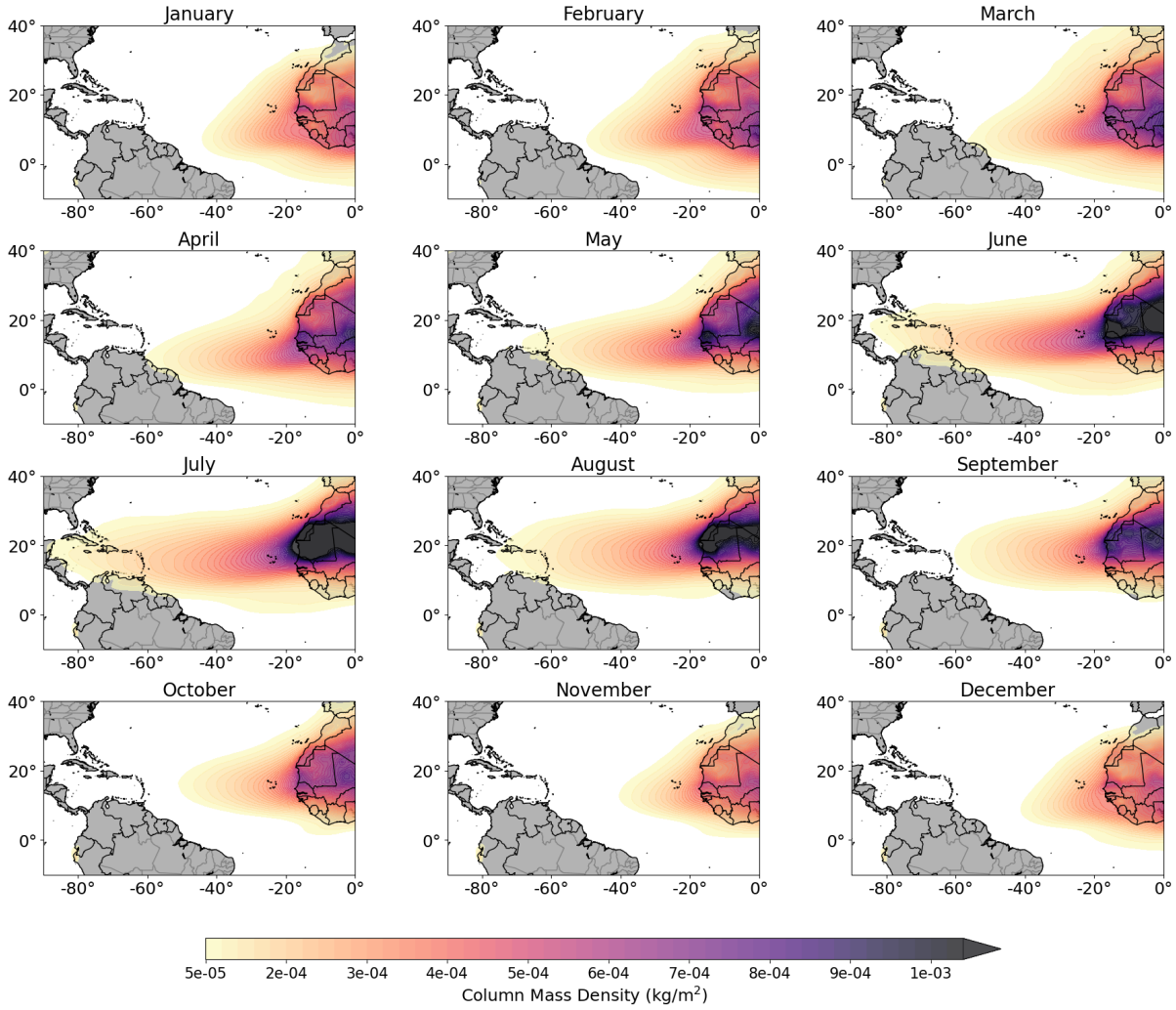

FIGURE 1.1: MERRA-2 monthly climatology of dust column mass density from 1980 to 2023.

1.2 Saharan Dust

1.2.1 Saharan Dust Transport and Modeling

Saharan dust is primarily transported into the Atlantic Ocean from the northwest coast of Africa via Saharan dust outbreaks. Approximately 10^{12} kg of dust is transported across the Atlantic each year, making North Africa the largest dust source in the world (Huang

et al., 2010). Saharan mineral dust particles range from 0.1 µm to 10 µm in radius, with the distribution of finer, further traveling transported mode dust peaking between 0.4 µm and 0.5 µm, whereas coarse mode particles peak in size distribution around 2 µm (Dubovik et al., 2002). The strength and location of Saharan dust storms depend strongly on the time of year. Such outbreaks can last for several days (Carlson, 1979), traveling at a speed of 8 to 10 degrees longitude per day (on the order of 1000 km/day), considerably affecting radiative heating in the atmosphere (Carlson and Benjamin, 1980). The location of Saharan dust outbreaks follows the season pattern of the inter-tropical convergence zone (ITCZ, Prospero et al., 1983). During the winter months, dust plumes travel off the west coast of Africa across the Atlantic to the northeastern coast of South America, centered between 5°N and 10°N. During the summer months, dust plumes shift northward and travel across the Atlantic into the Caribbean, centered around 17°N (Huang et al., 2010, Prospero et al., 1983, Swap et al., 1996). While the strongest dust outbreaks occur during June or July, outbreaks are common throughout the year, especially in winter, spring and summer (Huang et al., 2010). A reanalysis-based climatology of dust column mass density (mass density of dust in kg/m^3 integrated over height) from 1980 to 2023 is shown in Figure 1.1, and illustrates the seasonal shift in the location of dust outbreaks found in research over the past several decades. Saharan dust plumes are usually located below 5 or 6 km in altitude as they move off the West African coast in boreal summer (3 to 4 km in boreal winter) and decrease steadily in altitude during transport across the Atlantic, to below 3 km by the time they reach America (1 to 2 km in boreal winter) (Huang et al., 2010, Swap et al., 1996). The altitude of the dust layer is higher during

summer months than in winter months because of strong sensible heating causing low-level convergence over the Sahara which acts to lift the dust (Huang et al., 2010). The vertical distribution of the dust layer is a key factor in its radiative effects on the atmosphere (Carlson and Benjamin, 1980). Because of its strong absorptive properties, dust at the surface can increase daytime heating, and dust aloft can trigger temperature inversions (whereas a strongly scattering aerosol would cause cooling). Significant progress has been made in recent years in the development of precise 3-D aerosol models as well as in data assimilation of aerosol data for NWP. Such improvements have led to a more accurate and reliable representation of aerosols in NWP and reanalysis, significantly improving forecast accuracy (Mulcahy et al., 2014, Toll et al., 2016). These enhancements have allowed for more thorough research on aerosol effects on the atmospheric system. However, there remain many uncertainties in these effects, specifically in terms of atmospheric responses to aerosol effects. The effects of the physical properties of aerosols on weather patterns, especially on daily timescales, remain difficult to predict (Mulcahy et al., 2014, Toll et al., 2016, Zhang et al., 2016), due to limitations in aerosol characterization. Solving these issues remains a crucial step to improving the understanding and forecasting of the effect of mineral dust aerosols on the evolution of weather systems, especially in tropical regions.

1.2.2 Radiative Effects of Mineral Dust

Saharan dust affects Earth's radiation budget by both absorbing and scattering radiation. Scattering and absorption by aerosols are governed by the wavelength of incident radiation, particle size, and the complex refractive index of the particle, where the real

part of the refractive index is responsible for scattering and the imaginary part for absorption. For Saharan dust particles, these properties can depend on their size, mineral composition, and shape (Linke et al., 2006). The amount of scattering and absorption by aerosols depends on the absorption and extinction efficiencies which can be calculated using Mie theory, under the assumption of sphericity. The scattering and absorption properties of mineral dust therefore influence their interaction with shortwave (SW) and longwave (LW) radiation, which leads to negative or positive radiative forcing in the atmosphere depending on the single scatter albedo. The mineral composition of Saharan dust causes it to absorb both SW and LW radiation (Takemura et al., 2002), mainly due to the presence of hematite (Quijano et al., 2000), a dark-colored mineral with strong absorptive properties. The extinction properties of Saharan dust have been investigated in both laboratory studies and fieldwork. The extinction efficiency of mineral dust is almost constant in the solar band (Takemura et al., 2002). The single scatter albedo of mineral dust has been measured experimentally from field studies and found to range between 0.70 and 0.99 (Carlson and Benjamin, 1980, Eck et al., 1999, Takemura et al., 2002). The impact of Saharan dust has been found to be largest in the SW by Carlson and Benjamin (1980), which aligns with the findings of Grogan et al. (2016). SW radiation is found to cause strong heating within the dust layer, while strong LW heating is found to typically occur below the dust layer due to trapped outgoing LW radiation from the Earth (Carlson and Benjamin, 1980). A radiative transfer model (RTM) can be used to quantify the LW and SW effect of mineral dust on the atmosphere, by calculating SW and LW fluxes and heating rates.

1.3 African Easterly Waves

1.3.1 Development of African Easterly Waves

African Easterly Waves (AEWs) are synoptic systems that are generated over tropical North Africa due to a combined baroclinic and barotropic instability in the African Easterly Jet (Burpee, 1972, Charney and Stern, 1962). These disturbances in the jet propagate westward during the boreal summer (Burpee, 1972), and have been shown to be the main precursors of tropical cyclones (TCs) occurring in the North Atlantic basin (Landsea, 1993). AEWs have been understood to grow through a barotropic instability (Pytharoulis and Thorncroft, 1999) which evolves into a mixed barotropic–baroclinic instability (Burpee, 1972, Norquist et al., 1977, Pytharoulis and Thorncroft, 1999). However, increasing attention has been given to the role of heating in AEW genesis, as latent heating (Thorncroft et al., 2008) and SW and LW radiation (Ma et al., 2012) have been shown to play an important role in the development of these waves.

1.3.2 Influence of Saharan Dust on AEWs

The heating caused by Saharan dust has a direct impact on the energy balance of the atmosphere in the tropical East Atlantic where aerosol heating can reach several K/day (Ma et al., 2012). The effect of Saharan dust heating on the atmosphere in this region has been investigated over the last several decades, as the location of Saharan dust storms coincides with the development region of AEWs. However, the study of the effects of Saharan dust on the development of AEWs has yielded conflicting results. The effects of

Saharan dust are often studied in conjunction with the Saharan Air Layer (SAL), a layer of warm dry air that forms over the Saharan Desert and moves over the tropical North Atlantic Ocean. The dry air introduced by the SAL causes subsidence and stabilization of the atmosphere. This phenomenon has been observed to suppress the development of AEWs (Dunion and Velden, 2004, Pratt and Evans, 2009, Reale et al., 2009, Zipser et al., 2009). However, when the SAL is coupled with Saharan dust, the effects of this system on the atmosphere remain uncertain. Several studies have argued that Saharan dust plays a role in suppressing AEW development (Ismail et al., 2010, Jury and Santiago, 2010, Karyampudi et al., 1999). Other studies have found that Saharan dust can act to enhance AEW development (Grogan et al., 2016, Jones et al., 2004, Lavaysse et al., 2011, Ma et al., 2012). Recently, much work has been done in investigating how Saharan dust affects energy conversions in AEWs and impacts their development (Bercos-Hickey et al., 2017, Grogan et al., 2017, 2019, Grogan and Thorncroft, 2019, Grogan et al., 2022, Nathan et al., 2017). Grogan et al. (2016) specifically focuses on how interactions between the wave fields in dust, wind, and temperature are important to the growth and structure of AEWs, finding that dust effects increase baroclinic energy conversions (which are necessary to maintain the AEW), and that dust modified wave amplitudes are stronger at mid-levels but weaker at low levels of the atmosphere.

1.3.3 Current challenges and areas for further investigation

Past investigations into Saharan dust effects on AEWs have primarily relied on total aerosol optical depth (AOD), a measure of total extinction coefficient integrated over a

column in the atmosphere, to characterize the spatial distribution of dust. This limitation may contribute to the observed disparities in the conclusions of previous studies. A major constraint in these studies is the absence of investigation of the relationship between AEWs and alterations in the vertical distribution of dust aerosols. Further limitation arises from the failure to explicitly examine the dust impact throughout the development of the AEW into a TC. Previous research has been limited by the challenge of retrieving high-resolution measurements of vertical profiles of atmospheric parameters (moisture, wind, temperature) in Saharan dust events, particularly in the lower atmosphere, as most of these retrieval techniques are biased due to the presence of dust (Nalli et al., 2011, Oyola, 2015). Furthermore, accurate retrievals of aerosol vertical distribution are rare, and limited to satellite instruments such as the Cloud-Aerosol Lidar with Orthogonal Polarization (CALIOP), part of the Cloud-Aerosol Lidar and Infrared Pathfinder Satellite Observations (CALIPSO) mission (Winker et al., 2009), which is no longer operational, and rare observational measurements from field campaigns.

1.4 Research questions addressed in this study

Obtaining high-resolution aerosol profiles from observations has proven challenging, particularly over oceanic regions. However, when such data is available, it can contribute significantly to addressing unanswered questions. This work aims to combine high-resolution field campaign datasets, aerosol vertical profiles from reanalysis, and radiative transfer modeling to shed light on the importance of accounting for the vertical distribution of Saharan dust in the context of AEW development.

The following research questions are addressed:

1. What is the impact of anomalous dust loadings on modifying atmospheric heating rates at different atmospheric levels during AEW development?

2. Is this impact accurately captured in models such as reanalysis datasets?

3. How does the vertical structure of heating evolve throughout the development of an AEW?

To answer these questions, we integrate data collected during the airborne National Aeronautics and Space Administration (NASA) Convective Processes Experiment – Cabo Verde (CPEX-CV) and profiles from two different global reanalyses into a four-stream radiative transfer model. The CPEX-CV datasets provide a unique opportunity for this study, comprising collocated aircraft measurements of high-resolution vertical aerosol profiles and atmospheric profiles from dropsondes in the AEW development region. We examine radiative heating rates within Saharan dust plumes associated with AEWs during the field campaign for different dust concentration scenarios and evaluate dust radiative impacts in the context of AEW development.

Chapter 2

Methodology

2.1 Datasets

This study makes us of data obtained from the CPEX-CV field campaign collocated with data from two reanalyses: The Modern-Era Retrospective Analysis for Research and Applications, Version 2 (MERRA-2) and the Copernicus Atmosphere Monitoring Service (CAMS) to evaluate heating rates in the AEW development region using the Fu-Liou-Gu (FLG) radiative transfer model. The datasets ingested into this RTM are outlined below.

2.1.1 CPEX-CV

The CPEX-CV field campaign (Nowottnick et al., 2024) was conducted between 1 and 30 September 2022 out of Cabo Verde over the North Atlantic Ocean off the northwest coast of Africa. Its objectives included examining the interplay of atmospheric dynamics,

properties of the marine boundary layer, convection, the Saharan Air Layer and Saharan dust, and their interactions at different spatial scales. The mission aimed to enhance comprehension and predictive capabilities regarding the lifecycles of systems such as AEWs, aiming to increase understanding of such processes in this data-sparse region. During the field campaign, data were collected during thirteen research flights from the NASA DC-8 aircraft by several instruments including the ones described below. We utilize data from the seven research flights that coincided with an AEW that developed into a TC.

2.1.1.1 AVAPS Dropsondes

The Advanced Vertical Atmospheric Profiling System (AVAPS, Hock, 1999), is a dropsonde system providing vertical profiles of pressure, temperature, specific humidity, and winds that was used onboard the DC-8 during CPEX-CV. Dropsondes were launched at multiple locations during each flight. The profile altitude was limited to the DC-8 aircraft's maximum altitude of 42,000 ft, and most profiles did not contain data above 200 hPa. We employ 64 dropsonde profiles of pressure, temperature, and specific humidity throughout seven research flights to characterize atmospheric conditions in our analysis.

2.1.1.2 HALO

The NASA Langley High Altitude Lidar Observatory (HALO, Bedka et al., 2021) is a lidar system operated from an airborne platform to provide nadir-viewing profiles of water

vapor, methane columns, and aerosol and cloud optical properties. The HALO profiled the vertical distribution of aerosol in the atmosphere during each of the research flights used in our analysis. The 532 nm aerosol extinction coefficient, inferred from the aerosol backscatter (Carroll et al., 2022, Lei et al., 2022, Lenhardt et al., 2022) is used in our experiments as a measure of dust extinction coefficient. The latitude and longitude data from the HALO dataset were used to determine the flight track and location for each flight used in the analysis.

2.1.2 MERRA-2

MERRA-2 (Buchard et al., 2017, Gelaro et al., 2017, Randles et al., 2017) is a reanalysis dataset developed by NASA that provides comprehensive and high-quality atmospheric data from 1980 onward, including the assimilation of aerosols and a representation of their interactions with other physical processes. We utilize the 3D 6-hourly Analyzed Meteorological Fields dataset (or inst6_3d_ana_Nv on 72 levels) to generate profiles of pressure, temperature, specific humidity, and ozone mixing ratio. For aerosol profiles, we utilize the inst3_3d_aer_Nv collection, which includes instantaneous 3-dimensional 3-hourly data within MERRA-2. This dataset encompasses assimilated aerosol mixing ratio parameters at 72 model layers, including dust, sulfur dioxide, sea salt, black carbon, and organic carbon. Similarly, we also obtain 3-hourly AOD Analysis from the inst3_2d_gas_Nx.

Additional treatment is required in order to obtain extinction coefficient profiles from dust concentration. We calculate volume extinction coefficient at each level from dust mixing ratio for each of the five size-bins provided in the aerosol mixing ratio dataset,

using the following equation:

$$\beta_e = k_e \rho_{air} = \frac{3 R_{DU} Q_{ext}}{4 r \rho_p} \rho_{air} \tag{2.1}$$

where k_e is the mass extinction coefficient in $\mathrm{m^2\ kg^{-1}}$, ρ_{air} is the air density in $\mathrm{kg\ m^{-3}}$, R_{DU} is the dust mass mixing ratio for a specific bin in $\mathrm{kg\ kg^{-1}}$, Q_{ext} is the extinction efficiency, r is the particle radius in m, and ρ_p is the particle density in $\mathrm{kg\ m^{-3}}$. The air density is provided by the MERRA-2 analyzed meteorological fields. The particle radius used for each of the five size-bins is 0.73 μm, 1.4 μm, 2.4 μm, 4.5 μm, 8.0 μm respectively. The particle density is 2500 $\mathrm{kg\ m^{-3}}$ for particles of mean radius of 0.73 μm, and 2650 $\mathrm{kg\ m^{-3}}$ for the rest of the size-bins (GMAO, 2023). The extinction efficiency is approximated for each size-bin using values from the Goddard Chemistry Aerosol Radiation and Transport (GOCART) module (GMAO, 2023) that correspond to the closest particle radius for each bin. The total dust aerosol extinction coefficient is calculated from the sum across all size-bins. HALO data was assimilated into MERRA-2 for select flights, and dropsondes were assimilated into MERRA-2 across the entire campaign (Nowottnick et al., 2023), and our analysis sheds light on the performance of the assimilation.

2.1.3 CAMS

Because the CPEX-CV data were assimilated into the MERRA-2 reanalysis dataset used in this study, we use the CAMS reanalysis (Inness et al., 2019), which did not assimilate data from CPEX-CV, as a reference to assess the impacts of the observational

data assimilation on the reanalysis. CAMS is a reanalysis dataset that comprises 3D time-consistent atmospheric composition fields, including aerosols, chemical species, and greenhouse gases. We utilize the 3-hourly datasets on 25 pressure levels for temperature, specific humidity, and dust aerosol mixing ratio at three different particle size ranges (0.03 - 0.55 µm, 0.55 - 0.9 µm, 0.9 - 20 µm), as well as the total column AOD at 550 nm. Similar to the MERRA-2 dataset, we calculate the extinction coefficient at each level for the 3 dust size-bins listed above using the following formula:

$$\beta_e = k_e \rho_{air} = \frac{3 R_{DU} Q_{ext}}{4 r \rho_p} \cdot \frac{p}{R_d T_v} \tag{2.2}$$

where $T_v = (1 + 0.61q)T$ and p is the pressure in hPa, R_d is the gas constant for dry air in J kg^{-1} K^{-1}, T_v is the virtual temperature in K, q is the specific humidity in kg kg^{-1}, and T is the temperature in K. The pressure, specific humidity, and temperature are provided by the CAMS dataset. Since CAMS also uses GOCART aerosol properties, the values for extinction efficiency, particle radius, and particle density for each of the three size-bins are the same used for MERRA-2 for particle radii sizes of 0.24 μm, 0.8 μm, and 8 μm. Similarly to the MERRA-2 dataset, the values for extinction coefficient were summed to calculate the total dust aerosol extinction coefficient. Because each size-bin represents a range of particle sizes and the extinction efficiency depends on particle size, the accuracy of the extinction coefficient remains limited for both the MERRA-2 and CAMS datasets.

2.1.4 Fu-Liou-Gu Radiative Transfer Model

The Fu-Liou-Gu RTM calculates heating rates and irradiances (or fluxes) from profiles generated from the datasets described above. The FLG RT scheme, as proposed by Gu et al. (2011), represents an upgraded iteration of FLG originally developed by Fu and Liou in 1992 and 1993 (Fu and Liou, 1992, 1993). This refined model offers improved parameterizations for aerosol properties, which enable more accurate simulation of radiative effects, aligning more closely to real-world observations. The delta-four-stream approximation is utilized for solar radiative flux calculations (Liou et al., 1988) and the delta-two-and-four-stream approximation is employed for LW (or infrared, IR) radiative flux calculations (Fu et al., 1997) in the model. The model divides the SW and LW/IR spectra into 6 and 12 bands respectively, determined by the locations of absorption bands, and the calculations incorporate the effect of absorption by the H2O continuum and various minor absorbers within the solar spectrum in addition to the principal absorbing gases. The FLG RTM assumes the sphericity of aerosols, using Mie theory to model their optical properties. The mineral transported dust mode is used in this study to represent dust transported over the Atlantic. This mode favors smaller particles, able to remain suspended in the atmosphere over longer transport times.

2.1.4.1 OPAC

The current FLG radiation scheme contains a total of 18 aerosol types parametrized by the Optical Properties of Aerosols and Clouds (OPAC, Hess et al., 1998) database.

This database provides humidity-aware single-scattering properties for spherical aerosols computed from Lorenz Mie theory, for 60 wavelengths in the spectral region between 0.3 µm and 40 µm. These 60 bands are interpolated into the 18 bands of the FLG RT scheme. The 18 types of aerosol include maritime, continental, urban, five size-bins for mineral dust, insoluble, water soluble, soot (black carbon), sulfate droplets, sea salt in two modes (accumulation and coarse mode), and mineral dust in four different modes (nucleation, accumulation, coarse, and transported mode). For the purposes of this study, we employ the mineral dust transported mode.

2.1.5 AEW Tracking

2.1.5.1 Maps of Precipitation and Dust Mixing Ratio

To visualize the location of dust in relation to convection and precipitation, we superimpose daily maps of MERRA-2 total dust mixing ratio onto maps of daily accumulated precipitation (e.g. Figure 2.1). We use the Integrated Multi-satellitE Retrievals for Global Precipitation Measurement (IMERG, Huffman et al., 2020) a dataset developed and provided by NASA offering global precipitation data by merging and integrating data from the Global Precipitation Measurement (GPM) satellite constellation. The MERRA-2 total dust mixing ratio is derived by summing the dust mixing ratio from five distinct particle size-bins. The flight track from the research flight corresponding to the day plotted on each map was overlaid to show the location of data collection relative to the AEW. These maps provided valuable insights into the interplay between dust and AEWs. In the

process of our analysis, we leveraged these maps, in conjunction with the daily forecast reports from CPEX-CV to identify specific days of interest for our study. Furthermore, we utilized these maps to track the temporal evolution of dust concentration throughout the field campaign.

2.1.5.2 AEW Tracking

We use the AEW tracker described in Lawton et al. (2022) to track the center of several developing AEWs of interest. The tracker calculates curvature vorticity at 700 hPa using the nondivergent component of the 700-hPa wind averaged within a radius of 600 km of each grid point. We use the positional dataset which supplies an approximation of the location of the center of the AEW at a 6-hour time step to collocate the center of the AEW with the nearest MERRA-2 and CAMS reanalysis datasets.

2.2 Radiative Transfer Modeling

2.2.1 Data processing

We use the positional data from the CPEX-CV HALO dataset to collocate data from the two reanalyses (MERRA-2 and CAMS) with the CPEX-CV dataset. We process the AVAPS dropsonde data to select profiles of pressure, temperature, and specific humidity with sufficient information to be run in the FLG RTM. We generate profiles from MERRA-2 and CAMS reanalysis at the each dropsonde profile location. Similarly, we process extinction coefficient profiles from HALO to select profiles providing sufficient

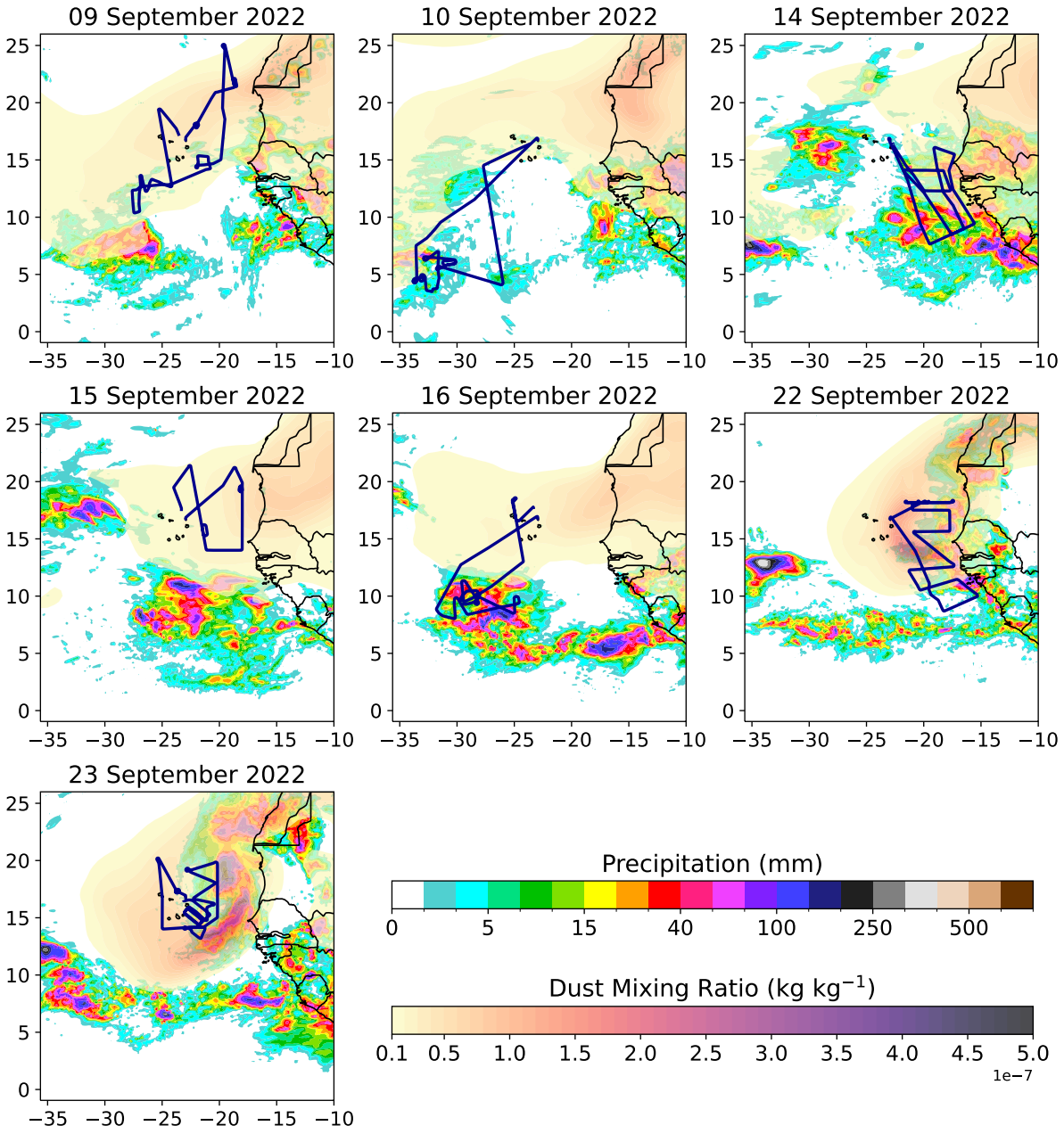

FIGURE 2.1: Flight tracks (blue) with overlaid total dust mixing ratio from MERRA-2 and daily accumulated precipitation from IMERG for seven of the research flights during the CPEX-CV field campaign.

aerosol extinction coefficient data to be run in the FLG RTM. We select extinction coefficient profiles from the HALO, MERRA-2, and CAMS datasets matching the location of the selected dropsonde profiles. We interpolate all profiles to 72 vertical levels, restricting

TABLE 2.1: FLG Input parameter datasets for PTQ (atmospheric profile of pressure, temperature, and humidity) and extinction coefficient (see text for further details on parameter calculations).

Dataset	PTQ	Extinction coefficient
CPEX-CV	AVAPS Dropsondes	HALO Extinction Coefficient
MERRA-2	6-hourly Analyzed Meteorological Fields	Extinction coefficient from 3-hourly Dust Mixing Ratio
CAMS	3-hourly pressure, temperature, specific humidity	Extinction coefficient from 3-hourly Dust Mixing Ratio

both the atmospheric and extinction coefficient profiles to below the 100 hPa level. Values of AOD are retrieved for each location using the 532 nm Total Optical Thickness from CPEX-CV, Aerosol Optical Depth Analysis from MERRA-2 and Total Aerosol Optical Depth at 550 nm from CAMS. These profiles, along with AOD values, are used for the calculation of heating rates using the FLG RTM. A summary of datasets used as inputs in the FLG RTM is given in Table 2.1. To investigate dust radiative effects in the context of different developing AEWs, we calculate a mean pressure, temperature and specific humidity profile from the AVAPS dropsonde dataset and a mean extinction coefficient profile from the HALO extinction coefficient dataset for each flight. We generate a corresponding mean atmospheric profile and extinction coefficient profile from both reanalyses using the collocated dataset. These mean profiles are used in the case study of daily mean heating rates during different developing AEW events.

2.2.2 FLG Input Parameters

Profiles of mean temperature in Kelvin (top row) and specific humidity in kg kg^{-1} (bottom row) which were utilized in the radiative transfer calculation are depicted in Figure 2.2. The shading shows the spread of all profiles ingested in the RTM, for both background and

anomalous aerosol concentrations. CPEX-CV data are shown in the left column (where temperature and humidity data are from the AVAPS dropsonde dataset), while the other two columns show the collocated mean profiles and corresponding spread obtained from MERRA-2 and CAMS reanalysis. The temperature profiles across the three datasets exhibit strong similarities. However, the specific humidity profiles exhibit more variability across the three datasets (CPEX-CV, MERRA-2, and CAMS), particularly below the 800 hPa level where values differ more strongly in range. Values in specific humidity drop lower in the CPEX-CV dataset than in the two reanalyses at the lower levels of the atmosphere. In the CAMS dataset, there is a sharp spike in specific humidity above 900 hPa on the lower end of the spread, whereas for MERRA-2, the values of humidity between 900 hPa and 750 hPa remain fairly consistent. This variability impacts heating rate profiles, which is especially noticeable at these levels for heating rates calculated from the CAMS dataset.

Profiles of aerosol extinction coefficient in km^{-1} for background AOD (top row) and anomalous AOD (bottom row) as defined in subsection 2.2.4 which were utilized in the radiative transfer calculation are depicted in Figure 2.3. The shading shows the spread of all profiles ingested in the RTM, for either the background and the anomalous AOD experiments. Once again, CPEX-CV data is shown in the left column (where extinction coefficient data is from the HALO dataset), while the other two columns show the collocated mean profiles and corresponding spread obtained from MERRA-2 and CAMS reanalysis. The extinction coefficient profiles exhibit more similarities across the three datasets in the background AOD case, with a peak near the surface and another in the

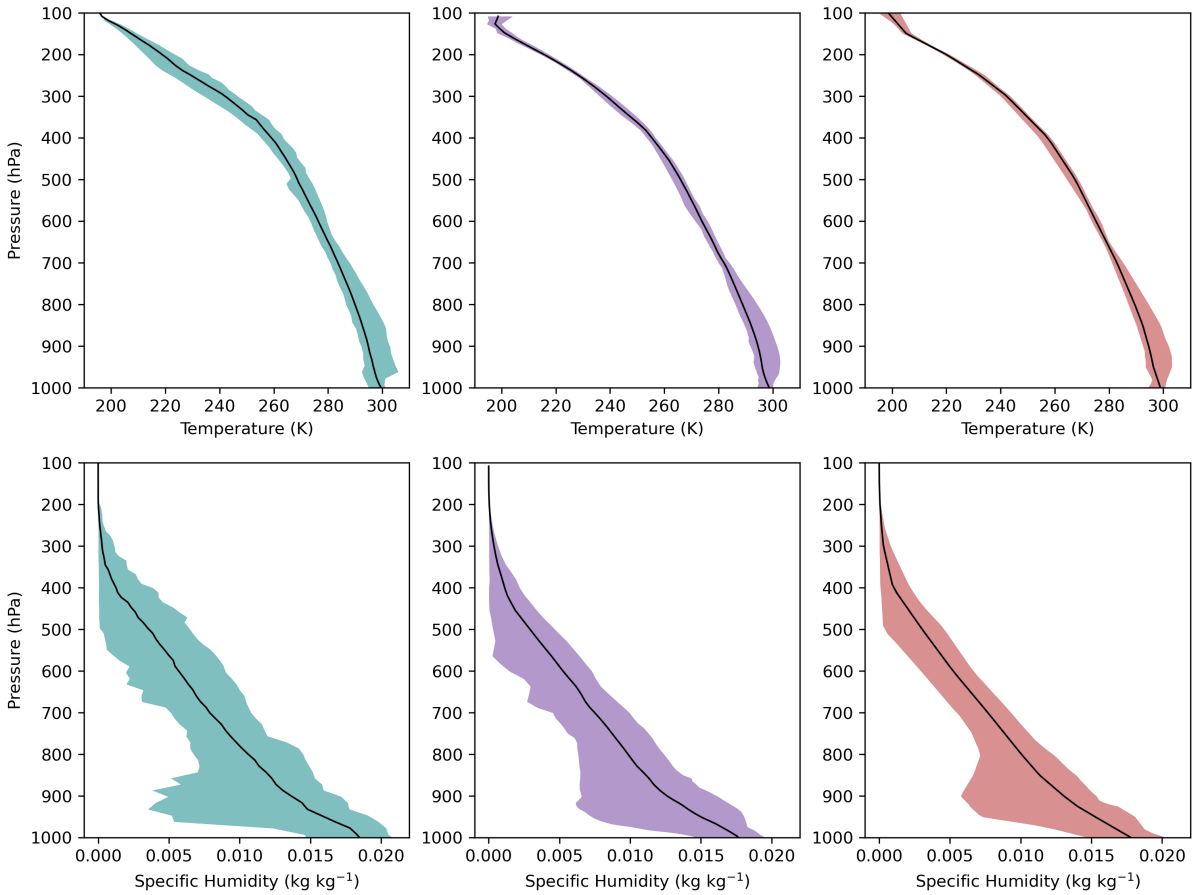

FIGURE 2.2: Temperature (top) and specific humidity (bottom) mean (black) and range for all CPEX-CV (teal), MERRA-2 (purple) and CAMS (red) profiles used in the study, including background and anomalous dust concentrations.

mid-levels of the atmosphere. However, in the anomalous AOD case, the extinction coefficient reaches much higher values (close to 4 km^{-1}) in the CPEX-CV dataset than in MERRA-2 and CAMS, which underestimate extinction coefficient by several K/day at several different levels of the atmosphere. The CPEX-CV observations of extinction coefficient are consistent with satellite observations in this area (Sauter et al., 2019).

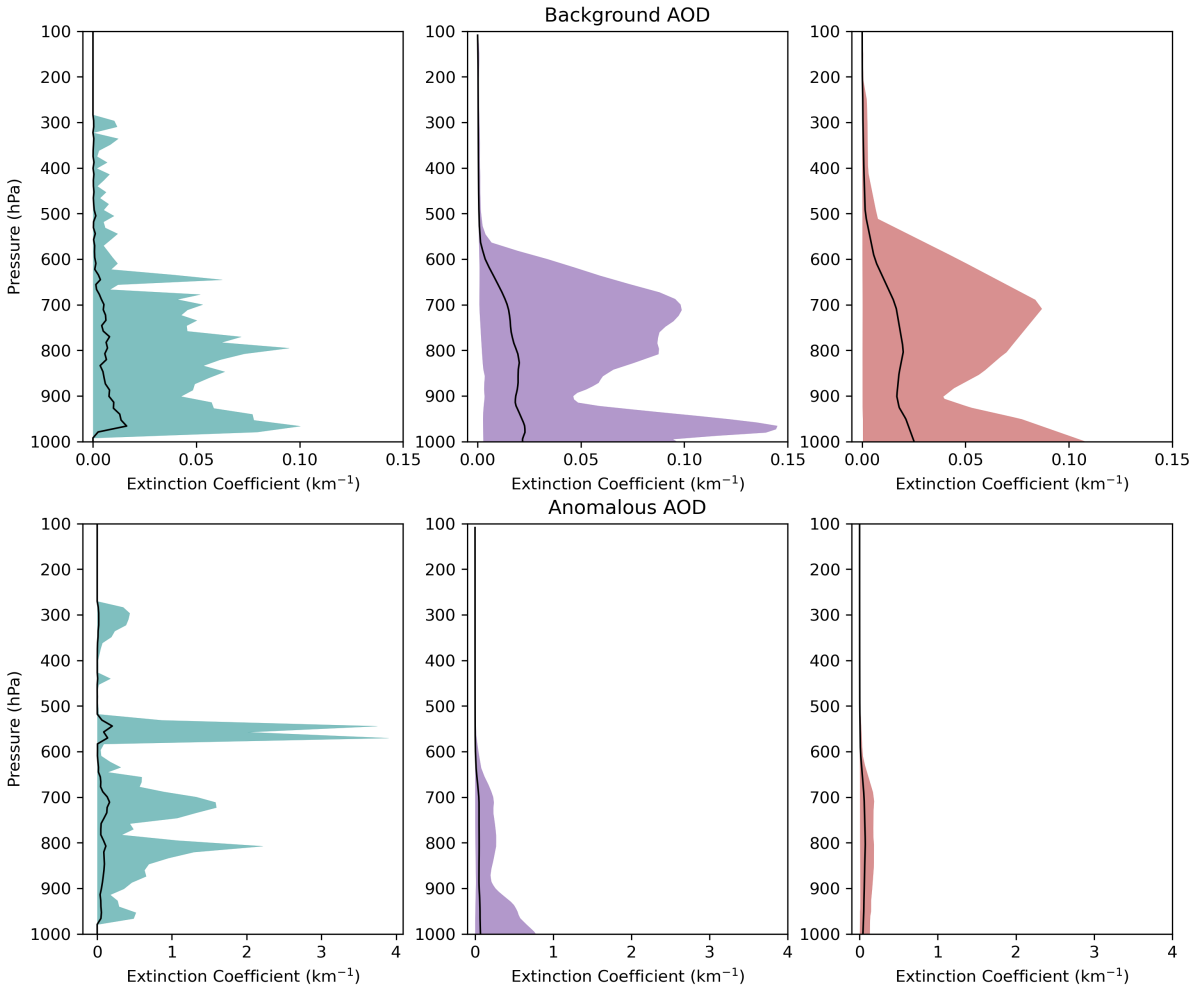

FIGURE 2.3: Extinction coefficient mean (black) and range for CPEX-CV (teal), MERRA-2 (purple) and CAMS (red) background AOD profiles (top) used in the study and anomalous AOD profiles (bottom), including background and anomalous dust concentrations (note the difference in the x-axis scale between the top and bottom panels).

2.2.3 Calculation of heating rates

Following a similar approach to Oyola et al. (2019), we run the FLG RTM ingesting atmospheric profiles from the three datasets (MERRA-2, CAMS, and CPEX-CV) to retrieve heating rates throughout the vertical layer at each of the selected dropsonde locations. Simulations are performed after accounting for the solar zenith angle at the corresponding local time and location. Heating rates are calculated in the FLG RTM by

an equation similar to Petty (2008):

$$\begin{aligned}\mathcal{H}(z) \equiv -\frac{1}{\rho(z)C_p}\Bigg\{ & -[F_i^{\uparrow}(0) - \Delta\tilde{v}_l\pi\bar{B}_l(z)]\frac{\partial\tau_i(0,z)}{\partial z} \\ & -[F_i^{\downarrow}(\infty) - \Delta\tilde{v}_l\pi\bar{B}_l(z)]\frac{\partial\tau_i(z,\infty)}{\partial z} \\ & -\Delta\tilde{v}_l\pi\int_z^{\infty}[\bar{B}_l(z') - \bar{B}_l(z)]\frac{\partial^2\tau_i(z,z')}{\partial z' dz}dz' \\ & -\Delta\tilde{v}_l\pi\int_0^{z}[\bar{B}_l(z') - \bar{B}_l(z)]\frac{\partial^2\tau_i(z',z)}{\partial z' dz}dz'\Bigg\}\end{aligned} \tag{2.3}$$

where $\rho(z)$ is the air density at level z, C_p= 1005 J kg^{-1} K^{-1} is the specific heat capacity of air at constant pressure, τ_i is the band average flux transmittance, $\tilde{v}_l$ represents the spectral interval or band (SW, LW/IR), $F_i^{\uparrow}$, $F_i^{\downarrow}$, $F_i^{\uparrow}(0)$, $F_i^{\downarrow}(\infty)$ are fluxes where the arrows represent the direction of incoming flow (from surface up from top of atmosphere to surface), and the indices 0 and ∞ represent the surface and TOA respectively. The heating rate is dominated in magnitude by the first two terms: the first term quantifies radiative exchange with the boundary layer and is generally a heating term, while the second term quantifies radiative exchange with the top of the atmosphere and thus predicts LW/IR cooling to space. In its summarized form, the heating rate equation can be stated as:

$$\mathcal{H}(z) \equiv -\frac{1}{\rho(z)C_p}\frac{\partial F_{net}}{\partial z} \tag{2.4}$$

Here, F_{net} is the net flux given by the difference between upward and downward-directed fluxes.

2.2.4 Heating rate experiments

We analyze the impact of dust on atmosphere heating during the seven research flights that coincided with an AEW that developed into a TC. We distinguish between background AOD and anomalous AOD to investigate the impact of dust concentration on atmospheric heating rates. We define a threshold of AOD ≤ 0.2, a standard AOD level below which the presence of aerosol is not considered anomalous. This threshold is determined from the CPEX-CV 532 nm total optical thickness to select background dust concentration profiles. We obtain 32 dropsonde locations which fit the condition of background AOD (AOD ≤ 0.2), and we collocate thermodynamic profiles and extinction profiles from all three datasets (MERRA-2, CAMS, CPEX-CV) at these locations. We then select the top 32 dropsonde locations with highest AOD calculated from CPEX-CV 532 nm total optical thickness and define these as anomalous dust concentration profiles, once again collocating profiles from the three datasets at each location. The minimum AOD that meets the anomalous criteria was 0.335. This approach results in an equal parts data split, where 50% of the profiles are labeled as anomalous or high dust, while the lower 50% was classified as low or background dust. The profiles selected for the background and anomalous cases for MERRA-2 and CAMS are based on the CPEX-CV AOD threshold, not MERRA-2 and CAMS AOD values: this results in the three datasets having differing distributions of AOD values corresponding to background and anomalous AOD. The distribution of AOD values for the background and anomalous cases for each dataset (CPEX-CV, MERRA-2, CAMS) is shown in Figure 2.4. A total of 64 different

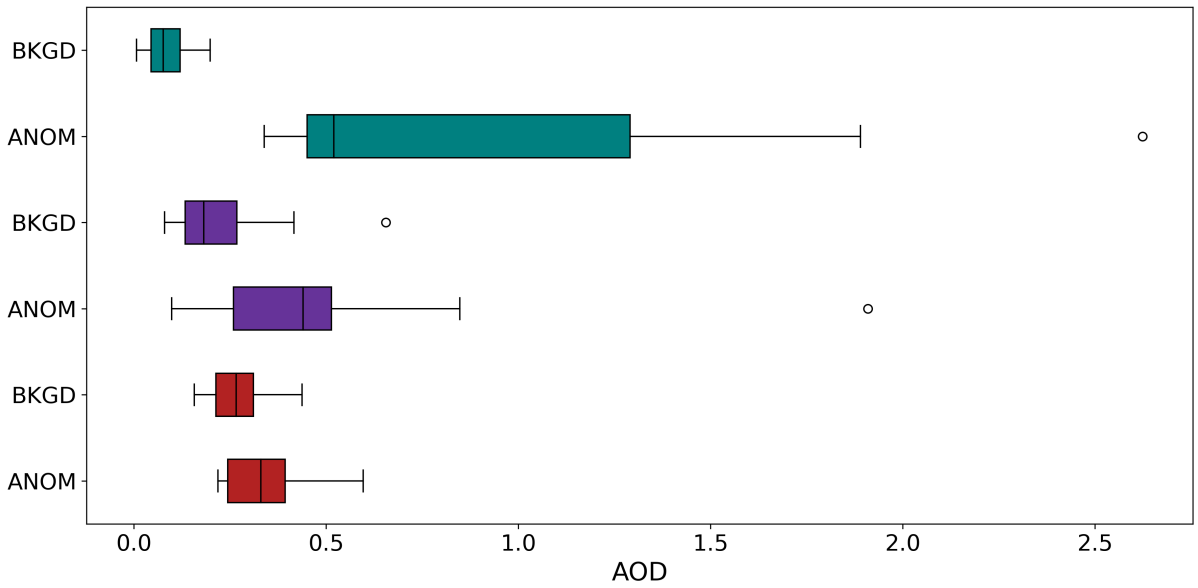

FIGURE 2.4: AOD Distribution for CPEX-CV (teal), MERRA-2 (purple) and CAMS (red) at the locations of the 32 profiles used in the background (BKGD) dust case and the 32 profiles used in the anomalous (ANOM) dust case.

profiles corresponding to CPEX-CV dropsonde deployment locations are thus selected, all within a developing AEW or its environment. For each one of these profiles, we run the FLG RTM for the three datasets (CPEX-CV, MERRA-2, and CAMS), and for each of them, two RTM runs are performed: one without the aerosol effect (the RTM only initialized with pressure, temperature, specific humidity, and ozone), which we refer to as the control run, and another one using the same initialization with an added aerosol extinction coefficient profile and corresponding AOD, which we refer to as the aerosol-aware run, for a total of 384 runs. We use the FLG RTM to calculate radiative fluxes (in W/m^2) and heating rates (in K/day) for each one of the 384 cases.

Chapter 3

Aerosol Heating in Reanalysis

3.1 Impact of Aerosol on Heating Rates

3.1.1 Methodology

The shortwave (SW), longwave/infrared (LW/IR), and total heating rate are calculated for 32 background AOD locations and 32 anomalous AOD locations in both a control run and and aerosol-aware run. A flowchart of the experiment is pictured in Figure 3.1. A mean SW, LW/IR and total heating rate are calculated for the background AOD case and for the anomalous AOD case for the control runs and aerosol aware-runs. To quantify the radiative effect of dust on atmospheric heating, the difference in heating between the aerosol-aware runs and the control runs is calculated. This results in a mean background

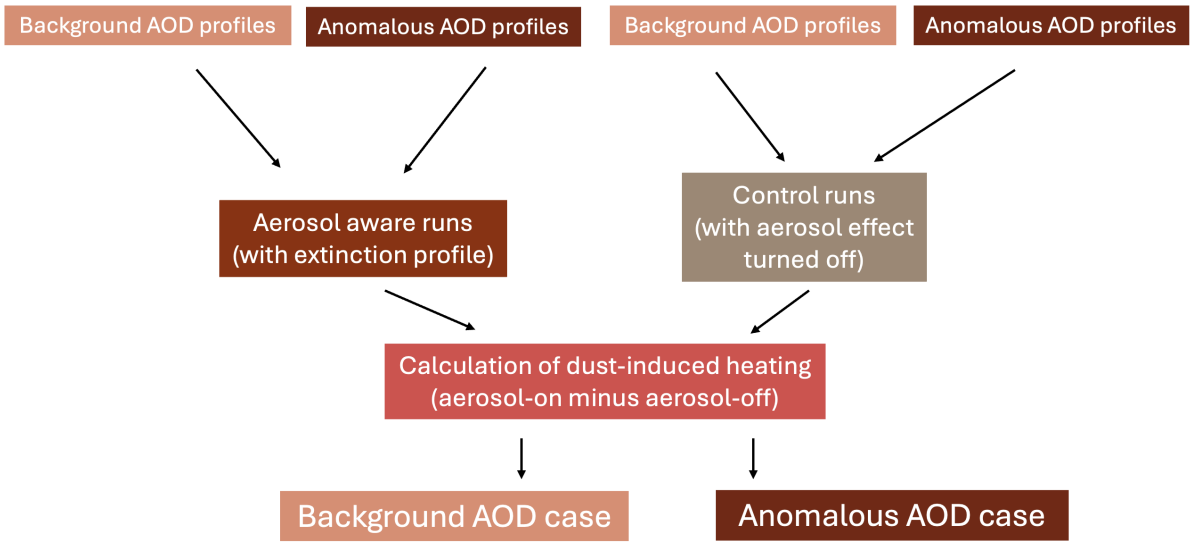

FIGURE 3.1: Flow chart of the experiment quantifying radiative effect of dust on atmospheric heating rates.

AOD profile for the control experiment and the aerosol-aware experiment and a mean anomalous AOD profile for the control experiment and the aerosol-aware experiment.

3.1.2 Background Aerosol Case

Figure 3.2 shows the mean heating rate differences (aerosol-aware minus control) for background AOD. Heating rate differentials are provided in three panels: SW, LW/IR, and total heating rate differences between the aerosol-aware run and the control run. Figure 3.2 reveals notable discrepancies between the reanalysis datasets and CPEX-CV in the calculated heating rate differences, particularly in the SW where differences are on the order of 1 to 2 K/day below 800 hPa. Both reanalysis profiles exhibit higher SW heating rates at the surface than CPEX-CV, exceeding 1 K/day, while the CPEX-CV heating is no larger than 0.4 K/day at the surface. The differences in SW heating rate profiles, especially at the lower levels of the atmosphere, can be attributed in part

to variations in aerosol vertical distribution and concentration, which are weighted by the input AOD. These differences in AOD are detailed in Figure 2.4, and show higher AOD values for the renalysis datasets than for CPEX-CV in the background AOD case. However, the peak in CAMS SW heating below 900 hPa was found to be driven by differences in the water vapor profile. This was tested by running the RTM with the CAMS extinction profile and a temperature and humidity profile from CPEX-CV, in which case the heating rate no longer displayed a large peak at those levels.

Most of the contribution to total heating rates comes from SW rather than IR. This is in part due to the fact that most of the CPEX-CV sampling used in this study occurred during the morning and close to solar noon, but is also an artifact of the choice of optical properties within the FLG RTM. Saharan dust, often composed of mineral-rich particles, is very active in the SW (Carlson and Benjamin, 1980). Consequently, the presence of Saharan dust in the atmosphere causes strong absorption of SW radiation, resulting in the localized heating effects we observe in the heating rate differential. The much smaller disparity observed between aerosol and control runs in the LW/IR radiation can be explained by the inherent characteristics of the optical properties for transported dust within the model. Unlike certain aerosols such as sulfates and nitrates that highly influence LW/IR radiation, mineral dust aerosols, including those from Saharan dust, tend to exhibit lower absorption efficiency in the LW/IR spectrum. The contribution of LW/IR radiation to radiative forcing is further limited by the dominance of the scattering effects of SW radiation by dust. Additionally, the interaction of various radiative forcing

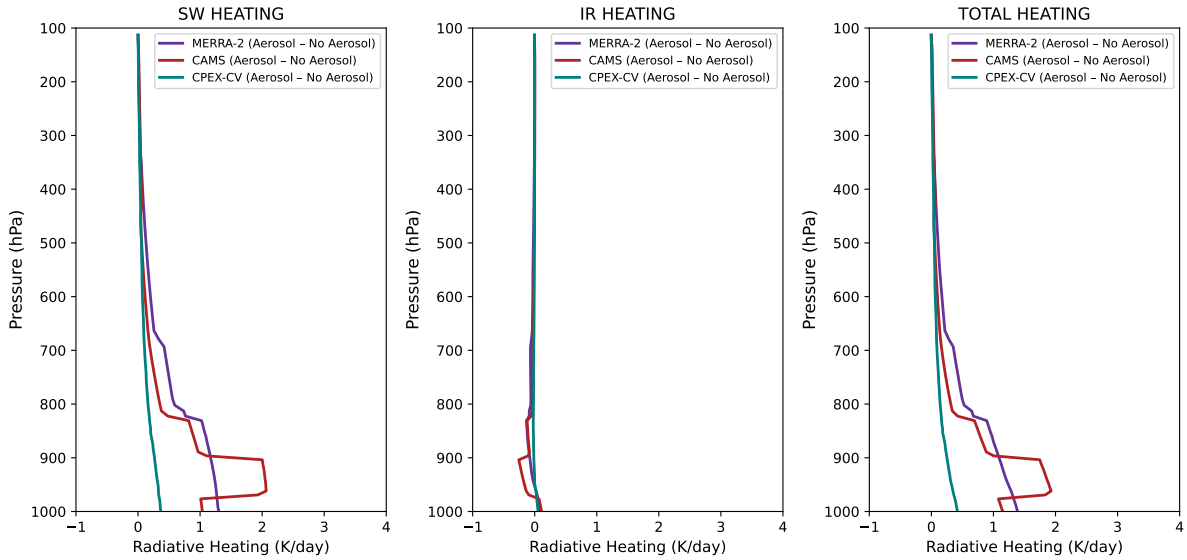

FIGURE 3.2: Heating rate difference between aerosol-aware and control run for MERRA-2 (purple), CAMS (red) and CPEX-CV (teal) for the background dust case. The left panel shows SW heating, the center panel shows LW/IR heating and the right panel shows total heating.

components, including water vapor and greenhouse gases, may overshadow the specific impact of dust aerosols in the LW/IR region.

3.1.3 Anomalous Aerosol Case

Figure 3.3 displays the same calculation as Figure 3.2 but for heating rates calculated for anomalous dust profiles with AOD exceeding 0.335 as defined previously. The impact of anomalous dust concentrations on heating rates is evident when compared with Figure 3.2; higher AOD values result in higher heating rates, specifically in the SW. The MERRA-2 SW heating difference reaches up to 2.2 K/day, while the CAMS SW heating rate difference reaches up to 3.8 K/day. Heating rates from reanalysis are higher than those calculated from CPEX-CV data below 800 hPa but lower than those calculated from

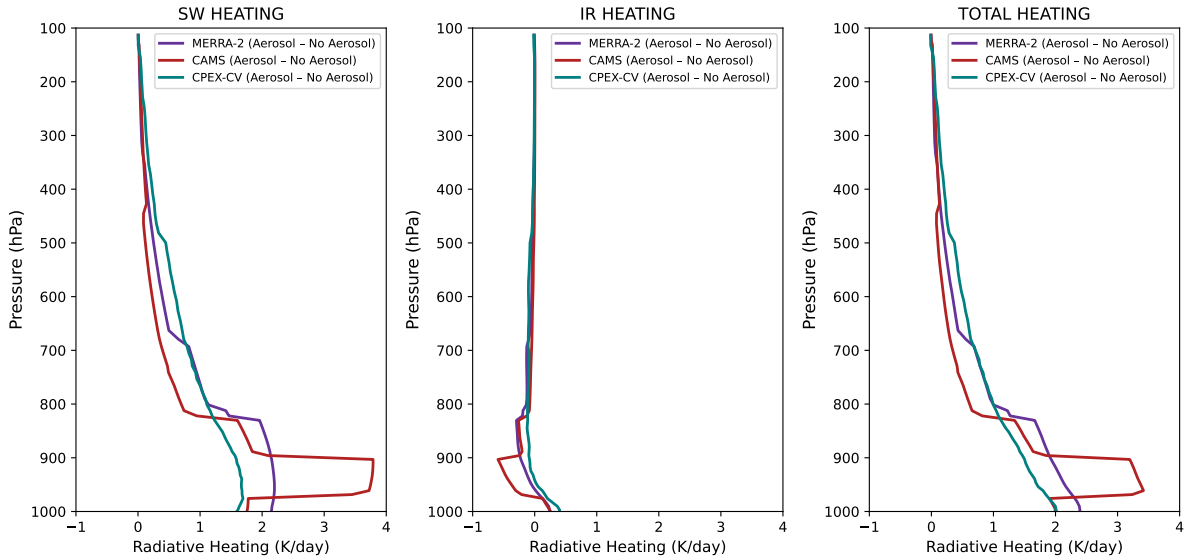

FIGURE 3.3: Heating rate difference between aerosol-aware and control run for MERRA-2 (purple), CAMS (red) and CPEX-CV (teal) for the anomalous dust case. The left panel shows SW heating, the center panel shows LW/IR heating and the right panel shows total heating.

CPEX-CV data between 700 and 250 hPa. The CPEX-CV observations of extinction coefficient for the anomalous case are consistent with multiple years of satellite observations (Sauter et al., 2019), showing that the heating rate differences in the anomalous case in September 2022 are not unusual and are likely present throughout time. The differences between reanalysis and CPEX-CV heating rates are shown in Figure 3.6 and Figure 3.7 and discussed below. There is also a notable increase in LW/IR cooling below 800 hPa in both MERRA-2 and CAMS in comparison with the findings in Figure 3.2, and an increase in LW/IR heating at surface levels. However, the impact of dust on total heating remains driven by the SW heating.

3.2 Comparative Analysis: The 2020 Godzilla Dust Storm

3.2.1 Methodology

To elucidate the differences in aerosol representation and subsequent impacts on heating rates between the MERRA-2 and CAMS reanalyses, specifically in the absence of cloud-related influences as encountered in the context of AEWs, we conducted a comparative analysis. This investigation focused on a notable event known as the Godzilla dust storm, an extreme dust storm that peaked on 18 June 2020 in a cloud-free environment within the same geographic region. Notably documented in the literature (Yu et al., 2021), the event showcased record AOD levels, as depicted in Figure 3.4 for 18 June 2020. Profiles from MERRA-2 and CAMS were generated at the respective grid point closest to 15 and 20 at 12:00Z. Values of AOD were 2.70 in the MERRA-2 reanalysis and 2.01 in CAMS. The FLG RTM was employed to compute heating rates from each of these profiles for an aerosol-aware run and a control run as described before. The difference in heating rates between the two runs was calculated to illustrate the aerosol impact on heating rates and is displayed in Figure 3.5.

3.2.2 Heating Rates in Extreme Dust Loading

The resultant aerosol impact, as illustrated in Figure 3.5, accentuates the high SW heating impact caused by heavy dust loading. However, the two reanalyses present differences in

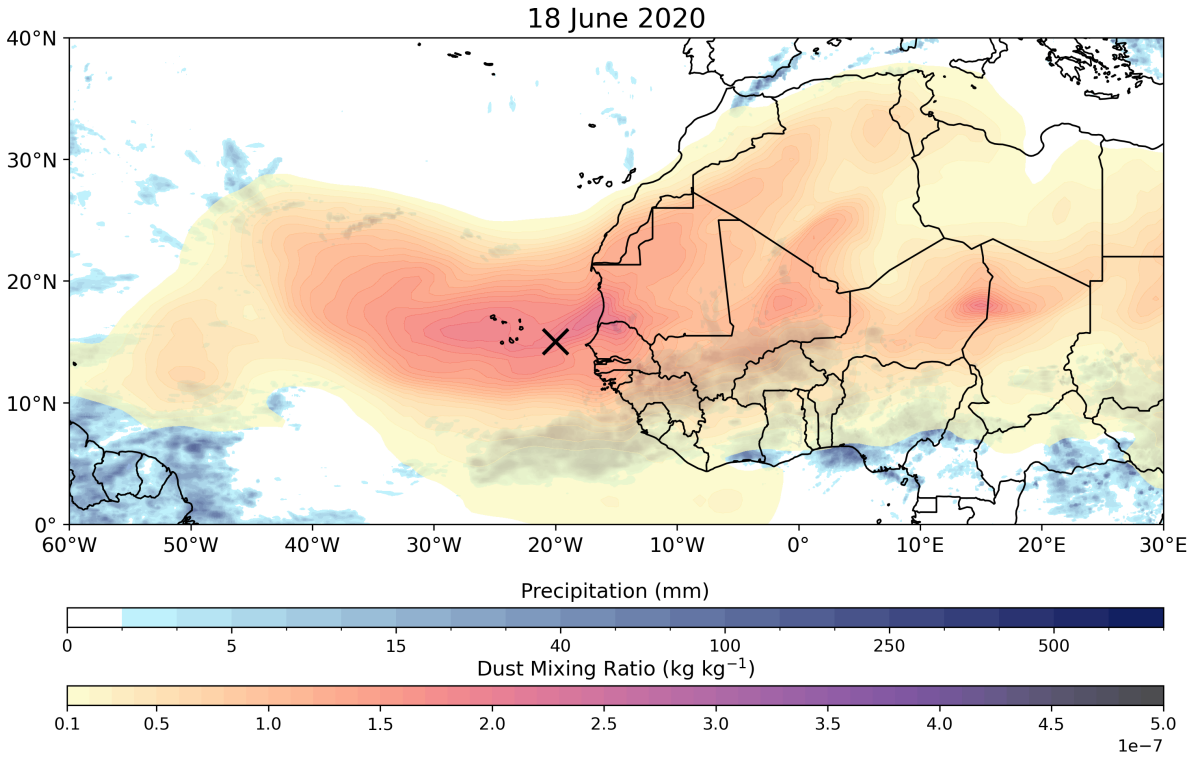

FIGURE 3.4: MERRA-2 total dust mixing ratio and IMERG daily accumulated precipitation on 18 June 2020. The location of the profile used in the analysis is marked in black.

the vertical distribution of heating. CAMS exhibits pronounced SW heating concentrated between 950 hPa and 900 hPa, while MERRA-2 displays lower peak values but a broader range extending from the surface to around 800 hPa. The heating is on the order of 4 times larger than in the anomalous dust loading profiles calculated for the CPEX-CV field campaign, which is driven by the substantially larger aerosol loading (see values of AOD for the respective cases). The peak in CAMS SW heating between 900 hPa and 950 hPa is driven by the water vapor profile, as was the case in Figure 3.2 and Figure 3.3. The LW/IR heating differences are positive at surface levels (2.5 K/day for MERRA-2, 1.5 K/day for CAMS), These values become negative above 950 hPa and remain near 0 K/day at higher levels in the atmosphere. The aerosol heating is thus mainly driven

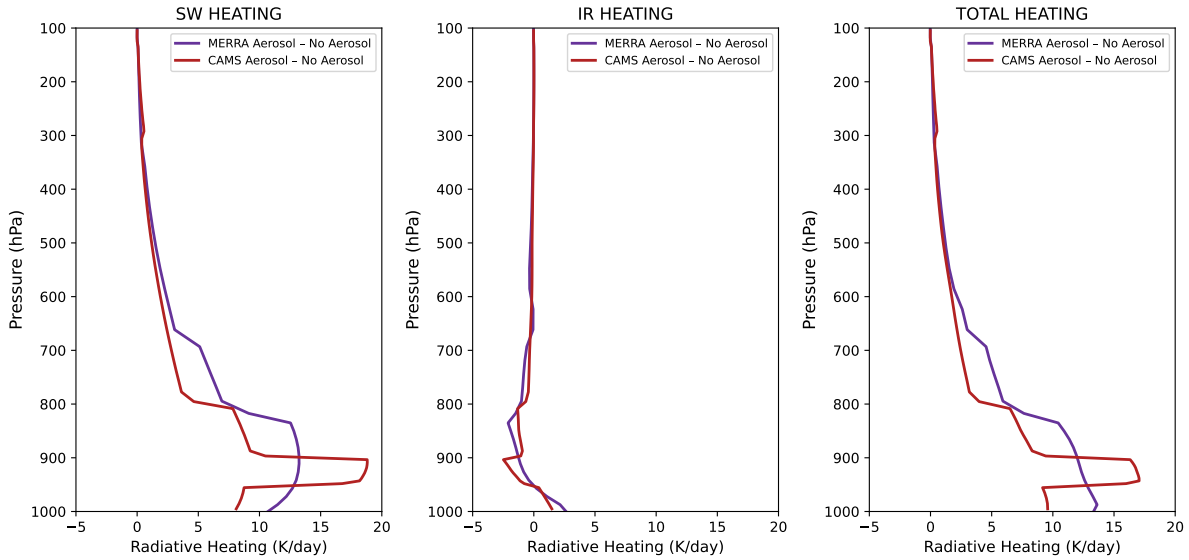

FIGURE 3.5: Heating rate difference between aerosol-aware and control run for MERRA-2 (purple) and CAMS (red) at 15, 20 on 18 June 2020. The left panel shows SW heating, the center panel shows LW/IR heating and the right panel shows total heating.

by SW radiation. The findings from this comparative analysis align with our analysis of heating rates during the CPEX-CV campaign, reinforcing the robustness of the observed profiles and the utility of the FLG RTM in capturing the nuances of aerosol-induced heating variations outside of cloud-influenced scenarios associated with AEWs.

3.3 Reanalysis Dataset Comparison

3.3.1 Methodology

Using the heating rate profiles calculated via the methodology described in subsection 3.1.1, we calculated the difference between heating rates from CPEX-CV and each reanalysis, for both the background aerosol and anomalous aerosol case. This resulted

in four measurements: the difference between MERRA-2 and CPEX-CV for the background aerosol case, the difference between CAMS and CPEX-CV for the background aerosol case, the difference between MERRA-2 and CPEX-CV for the anomalous aerosol case, and the difference between CAMS and CPEX-CV for the anomalous aerosol case. This experiment allowed us to examine the impact of the assimilation of CPEX-CV data into the MERRA-2 reanalysis, by comparing MERRA-2 outputs with CAMS, which did not include any assimilation of CPEX-CV data. This comparison is studied in both a background AOD scenario and an anomalous AOD scenario.

3.3.2 Background Aerosol Case

The differences between CPEX-CV and reanalysis for background AOD (AOD ≤ 0.2) are depicted in Figure 3.6, where the purple line represents the heating rate difference between MERRA-2 and CPEX-CV (MERRA-2 minus CPEX-CV), and the red line represents the heating rate difference between CAMS and CPEX-CV (CAMS minus CPEX-CV). The solid lines correspond to the aerosol-aware run, while the dotted lines represent the control run.

For the MERRA-2 background AOD case in Figure 3.6, the difference in SW heating reaches 0.9 K/day at the surface in the aerosol-aware run (solid purple line), and drops considerably around 825 hPa. The largest dust-induced SW heating differences between MERRA-2 and CPEX-CV are thus at these lower levels of the atmosphere. The control run SW profile is close to 0 K/day at those levels for MERRA-2, meaning that the heating shown in the aerosol-aware run is mainly driven by aerosol forcing. Strong differences in

LW/IR heating are seen for MERRA-2 in the mid-level atmosphere, exceeding 1.55 K/day around 600 hPa. The control run LW/IR profiles are very similar to the aerosol-aware profiles, and thus the differences between MERRA-2 and CPEX-CV cannot be attributed to aerosol forcing.

For background AOD, the SW heating difference between CAMS and truth is at its highest around 1.7 K/day between 975 hPa and 900 hPa in the aerosol-aware run. This discrepancy with MERRA-2 is mainly driven by differences in the CAMS humidity profile at this atmospheric level. Once again, the control run SW profile is close to 0 K/day in the areas of strongest SW heating for CAMS, showing that overall the SW heating is mainly driven by aerosol interactions. Large discrepancies in LW/IR between CAMS and truth are evident between 700 hPa and 500 hPa for both aerosol-aware and control runs, reaching up to 0.75 K/day for background AOD. The LW/IR heating difference between CAMS and CPEX-CV is smaller between 700 hPa and 550 hPa than the one observed between MERRA-2 and CPEX-CV, but is larger above 500 hPa. However, these differences are not driven by differences in dust aerosol profiles since there are minimal differences between the control run and the aerosol-aware run.

3.3.3 Anomalous Aerosol Case

The differences between CPEX-CV and reanalysis for anomalous AOD are depicted in Figure 3.7, where the purple line represents the heating rate difference between MERRA-2 and CPEX-CV (MERRA-2 minus CPEX-CV), and the red line represents the heating rate difference between CAMS and CPEX-CV (CAMS minus CPEX-CV).

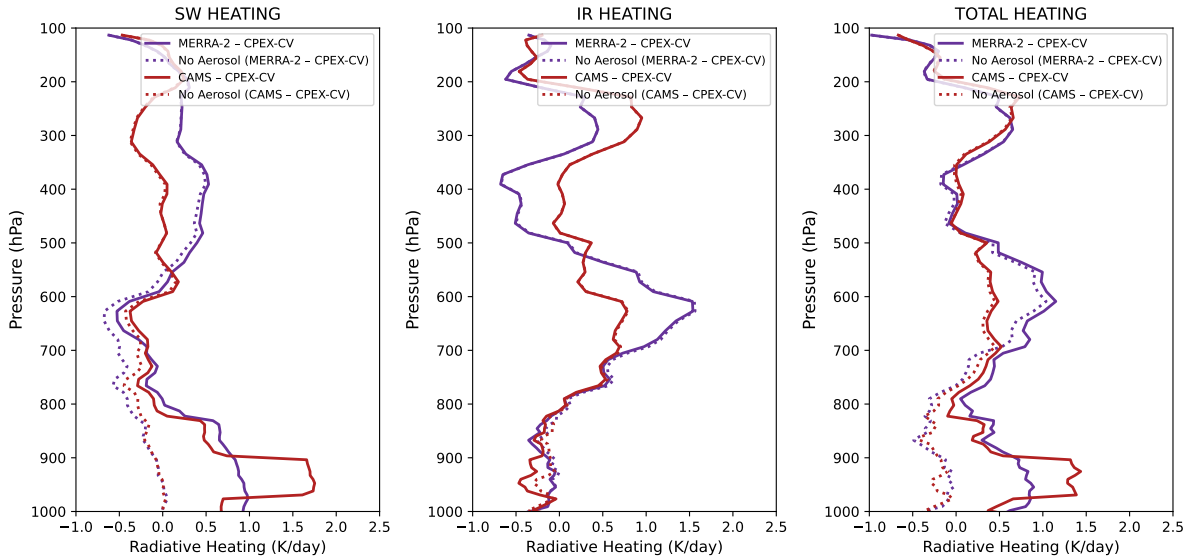

FIGURE 3.6: Heating rate difference between reanalysis and observation for the background dust case. Differences between MERRA-2 and CPEX-CV are plotted in purple and differences between CAMS and CPEX-CV are plotted in red. The solid lines correspond to the aerosol-aware run and the dotted lines correspond to the control run.

For MERRA-2, the aerosol-aware run exhibits a similar SW heating structure to the background dust profile in Figure 3.6 below 825 hPa, but with a lower maximum heating value of 0.6 K/day at the surface. This suggests that MERRA-2 represents the the observational data better at higher dust concentrations, since the difference between CPEX-CV and MERRA-2 is smaller in the anomalous AOD case. The LW/IR heating profile exhibits similar features to the background dust case depicted in Figure 3.6, consistent with the fact that dust does not interact as much with LW/IR radiation.

The SW heating difference between CAMS and CPEX-CV is around 2.05 K/day between 975 hPa and 900 hPa in the aerosol-aware run, which is higher than for the background AOD case. Unlike MERRA-2, CAMS SW heating is further from observation in the

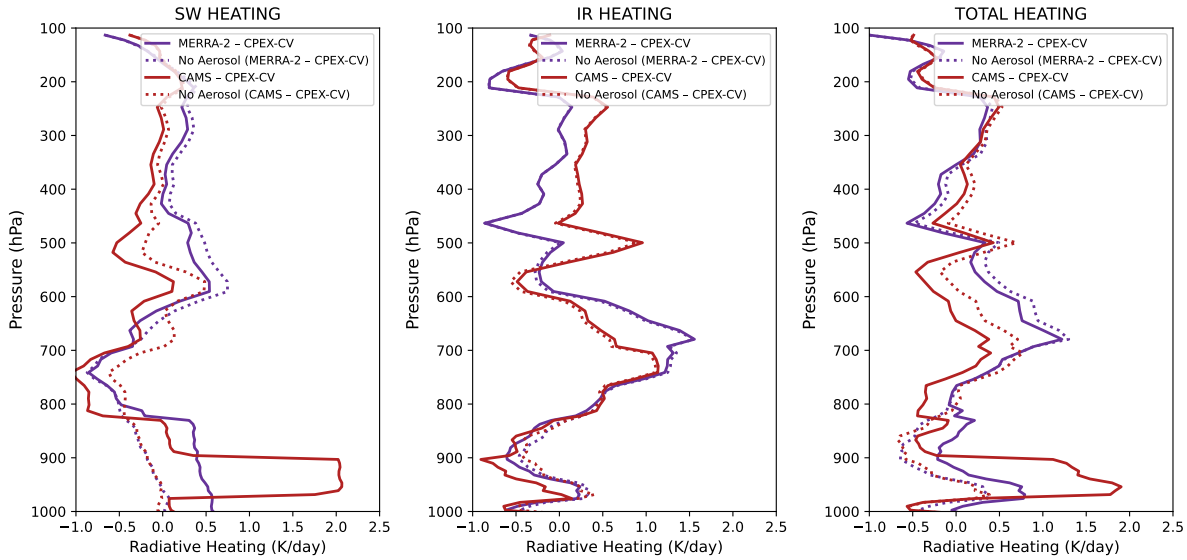

FIGURE 3.7: Heating rate difference between reanalysis and observation for the anomalous dust case. Differences between MERRA-2 and CPEX-CV are plotted in purple and differences between CAMS and CPEX-CV are plotted in red. The solid lines correspond to the aerosol-aware run and the dotted lines correspond to the control run.

anomalous AOD case than in the background AOD case, with differences with observation nearly 4 times larger than MERRA-2. As mentioned above, the discrepancy with MERRA-2 at these lower levels is mainly driven by the CAMS humidity profile. Large discrepancies in LW/IR between CAMS and CPEX-CV are evident between 700 hPa and 500 hPa for both aerosol-aware and control runs, reaching up to 1.2 K/day. The LW/IR heating difference between CAMS and CPEX-CV is smaller between 700 hPa and 550 hPa than the one observed between MERRA-2 and CPEX-CV, but is larger above 500 hPa. However, as mentioned previously, these differences are not likely driven by errors in dust aerosol characterization since there are minimal differences between the control run and the aerosol-aware run.

A major result from Figure 3.6 and Figure 3.7 is that despite the assimilation of CPEX-CV data into the MERRA-2 reanalysis dataset, large errors in SW heating rates persist throughout the atmosphere between MERRA-2 and what was observed during CPEX-CV. The average aerosol-aware MERRA-2 SW heating difference with CPEX-CV is 0.37 K/day, and the average aerosol-aware CAMS SW heating difference with CPEX-CV is 0.54 K/day. While MERRA-2 performs better than CAMS at representing observations, heating rate differences of the magnitude shown in these figures have a non-negligible impact on the atmosphere and cannot be ignored.

Chapter 4

Developing AEW Case Study

4.1 Overview of AEW events leading to named storms during CPEX-CV field campaign.

During the CPEX-CV field campaign, the thirteen DC-8 research flights sampled 10 different AEWs identified as AEW 1 through AEW 10. Four of these waves developed into named tropical storms (AEW 4, 5, 6, 8), with two intensifying into hurricanes (AEW 4, 6). We analyze three cases where the DC-8 flew in proximity to the AEW which later developed into a named storm: Fiona, Ian and Hermine. The progression and development of these AEWs were identified by the CPEX-CV team and verified using the AEW tracker described in Lawton et al. (2022).

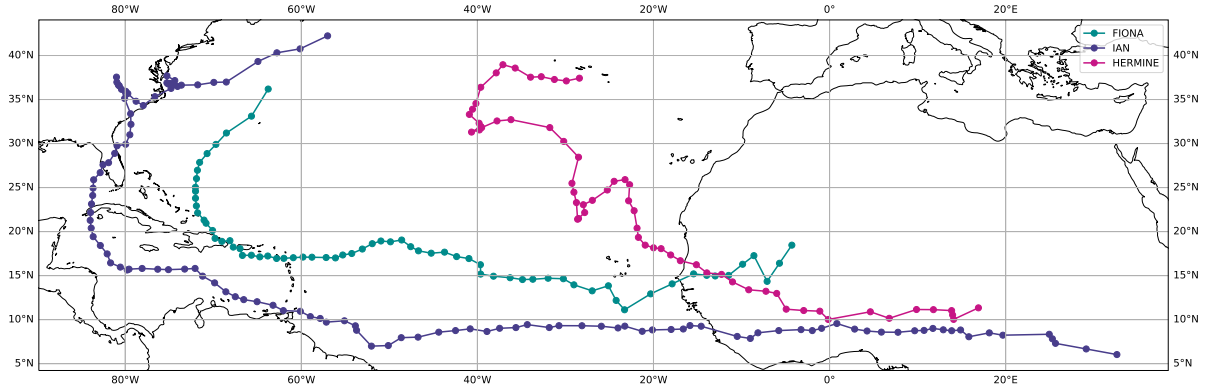

FIGURE 4.1: Tracks for AEWs leading to Hurricane Fiona, Hurricane Ian and TS Hermine.

4.1.1 AEW 4 / Fiona

On 07 September 2022, AEW 4 moved off the west coast of Africa and was located in the area of the CPEX-CV flight on 09 September 2022. As it progressed west, it evolved into Tropical Storm Fiona on 14 September 2022 and intensified into a hurricane on 18 September 2022. Fiona reached Category 4 with the highest 1-minute sustained winds of 140 mph (220 km/h) and produced catastrophic damage to many islands in the Caribbean (National Hurricane Center, 2022c). On 23 September 2022, it transitioned into an extra-tropical cyclone, directly impacting the Atlantic portion of Canada and becoming the costliest cyclone in Canadian history. It finally dissipated on 27 September 2022 (National Hurricane Center, 2022c). The DC-8 aircraft sampled the early stages of this storm on 09 September 2022, and the resulting data are analyzed in our study. Figure 4.2 shows the DC-8 flight track on that day, overlaid with MERRA-2 dust mixing ratio and IMERG daily accumulated precipitation.

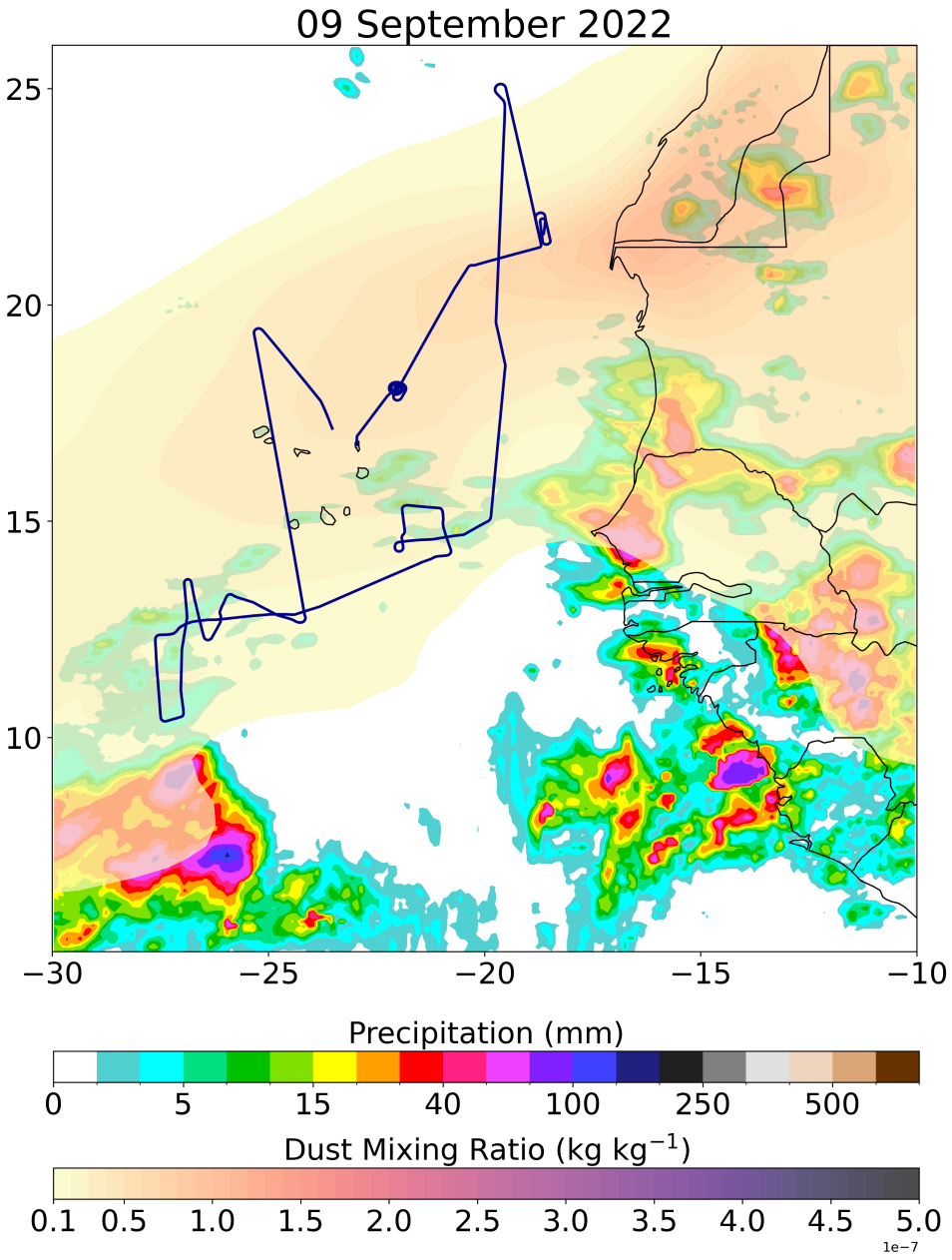

FIGURE 4.2: CPEX-CV DC-8 flight track (blue) with overlaid total dust mixing ratio from MERRA-2 and daily accumulated precipitation from IMERG on 09 September 2022.

4.1.2 AEW 6 / Ian

AEW 6 began moving off the west coast of Africa on 14 September 2022, coinciding with a CPEX-CV flight in the vicinity of the wave. The storm progressed west and transformed

into Tropical Storm Ian on 24 September 2022 and intensified into a hurricane on 26 September 2022 (National Hurricane Center, 2022a). The research flight on 14 September 2022 flew between AEW 5 (which later became TS Gaston) and AEW 6. The DC-8 flight track is pictured in Figure 4.3.

4.1.3 AEW 8 / Hermine

On 22 September 2022, AEW 8 moved off the African coast and intensified much more rapidly than Fiona and Hermine by turning into Tropical Storm Hermine a day later on 23 September 2022 (National Hurricane Center, 2022b). However, this hurricane was short-lived and weakened to a tropical depression on 24 September 2022. This storm, coinciding with the highest concentrations of Saharan dust sampled during the CPEX-CV field campaign, was sampled on 22 and 23 September 2022. The DC-8 flight track on 22 September 2022 is shown in Figure 4.4.

4.2 Aerosol heating in early stages of the AEWs

4.2.1 Methodology

We analyze the effect of aerosol on heating rates in the early stages of the AEW, comparing all three datasets (CPEX-CV, MERRA-2 and CAMS) on the three days of interest corresponding to the sampling of the early stages of Pre-Fiona, Pre-Ian and Pre-Hermine (09 September 2022, 14 September 2022 and 22 September 2022, respectively). The RTM simulations are performed after accounting for the solar zenith angle (SZA) at the mean

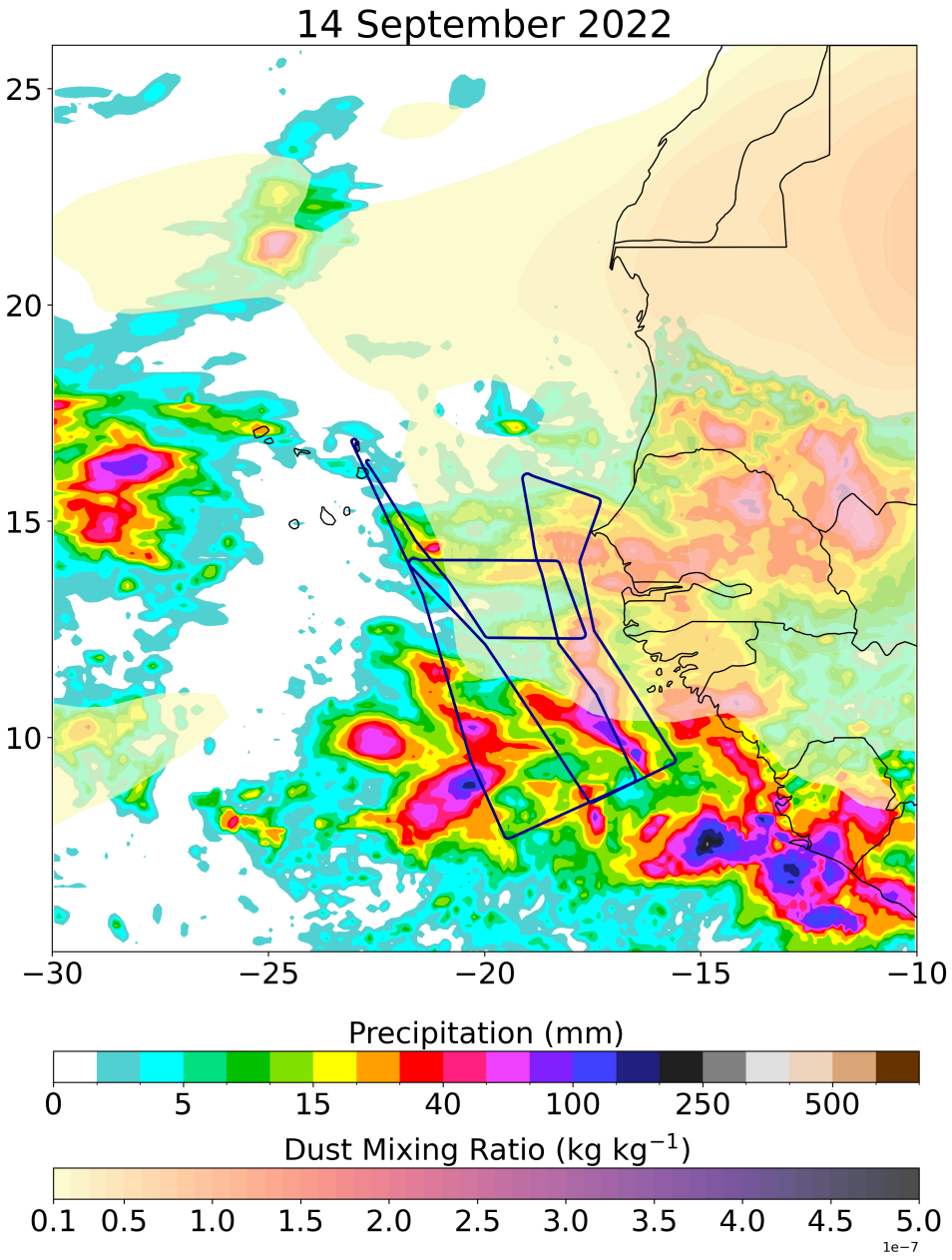

FIGURE 4.3: CPEX-CV DC-8 flight track (blue) with overlaid total dust mixing ratio from MERRA-2 and daily accumulated precipitation from IMERG on 14 September 2022.

local time and location of the flight which are listed in Table 4.1. Table 4.2 shows the mean, maximum, and standard deviation of AOD on the three case study days measured by the three datasets used in the case study, where the MERRA-2 and CAMS values

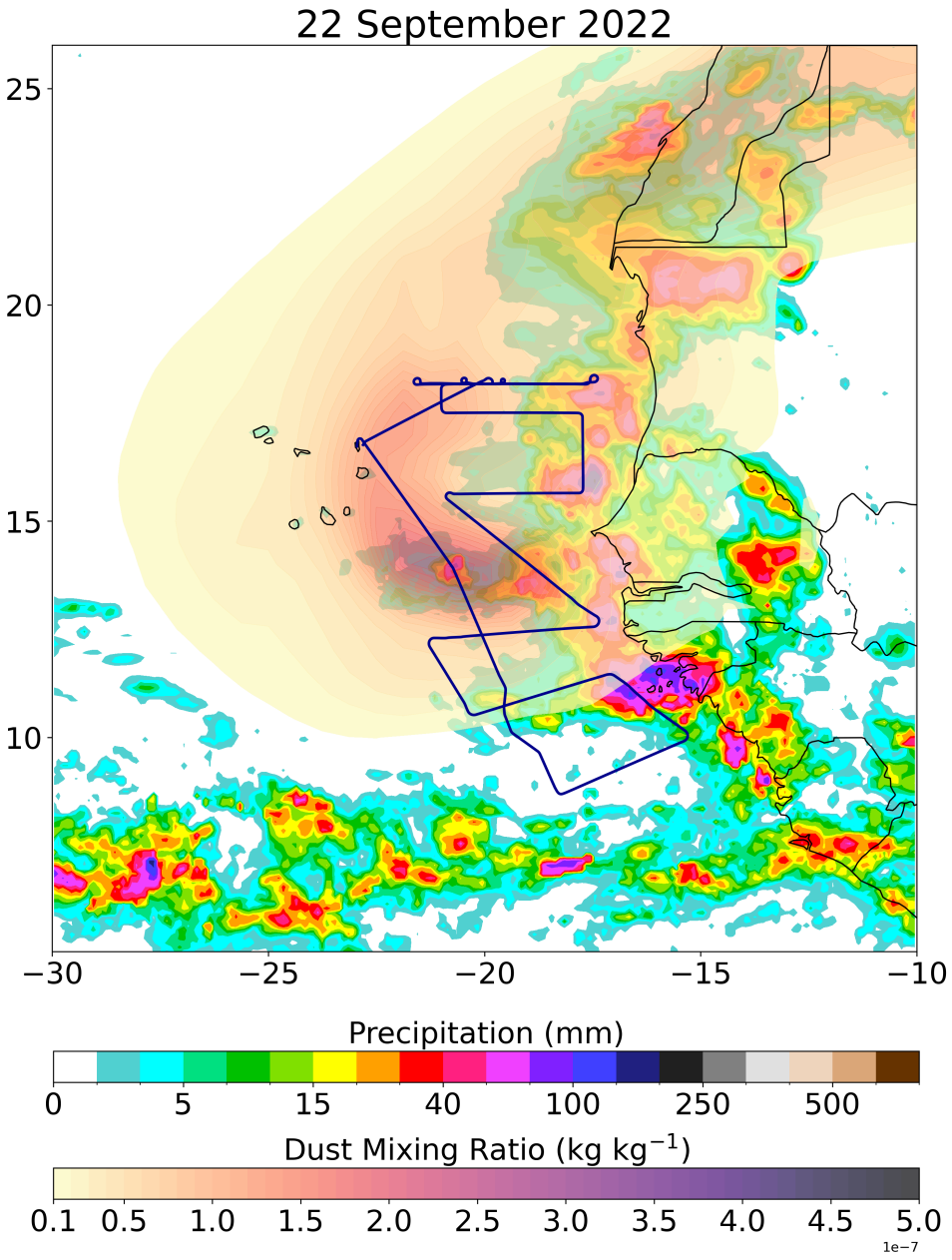

FIGURE 4.4: CPEX-CV DC-8 flight track (blue) with overlaid total dust mixing ratio from MERRA-2 and daily accumulated precipitation from IMERG on 22 September 2022.

are calculated from the collocation with the CPEX-CV flight path. The mean AOD was highest for the three datasets on 22 September 2022, and is most pronounced in the CPEX-CV dataset. Of note is also the maximum AOD of 3.34 measured by CPEX-CV,

TABLE 4.1: Coordinates and time used to calculate SZA in FLG RTM.

Case Study Day	Latitude	Longitude	Time (UTC)
09 September 2022	17.11°N	22.49°W	16:30
14 September 2022	12.54°N	19.41°W	12:00
22 September 2022	14.85°N	19.55°W	09:00

TABLE 4.2: Mean, maximum and standard deviation of AOD for CPEX-CV, MERRA-2 and CAMS on 09, 14 and 22 September 2022.

	09 September 2022			14 September 2022			22 September 2022		
Dataset	Mean	Max	STD	Mean	Max	STD	Mean	Max	STD
CPEX-CV	0.25	1.69	0.16	0.06	1.02	0.07	1.02	3.34	0.64
MERRA-2	0.33	0.72	0.16	0.23	0.63	0.10	0.59	2.49	0.48
CAMS	0.32	0.69	0.17	0.22	0.55	0.08	0.59	1.30	0.34

which is considerably larger than the maximum AOD in the MERRA-2 dataset (2.49) and the CAMS dataset (1.30) on 22 September 2022. As described in subsection 3.1.1, the FLG RTM is run for all 3 datasets (CPEX-CV, MERRA-2, and CAMS), and for each of them, two RTM runs are performed: one without the aerosol effect (RTM only initialized with pressure, temperature, specific humidity, and ozone), which we refer to as the control run, and another one using the same initialization with an added aerosol extinction coefficient profile and corresponding AOD, which we refer to as the aerosol-aware run. The aerosol-induced heating rate is then calculated by taking the difference between the aerosol-aware heating rate and control run heating rate.

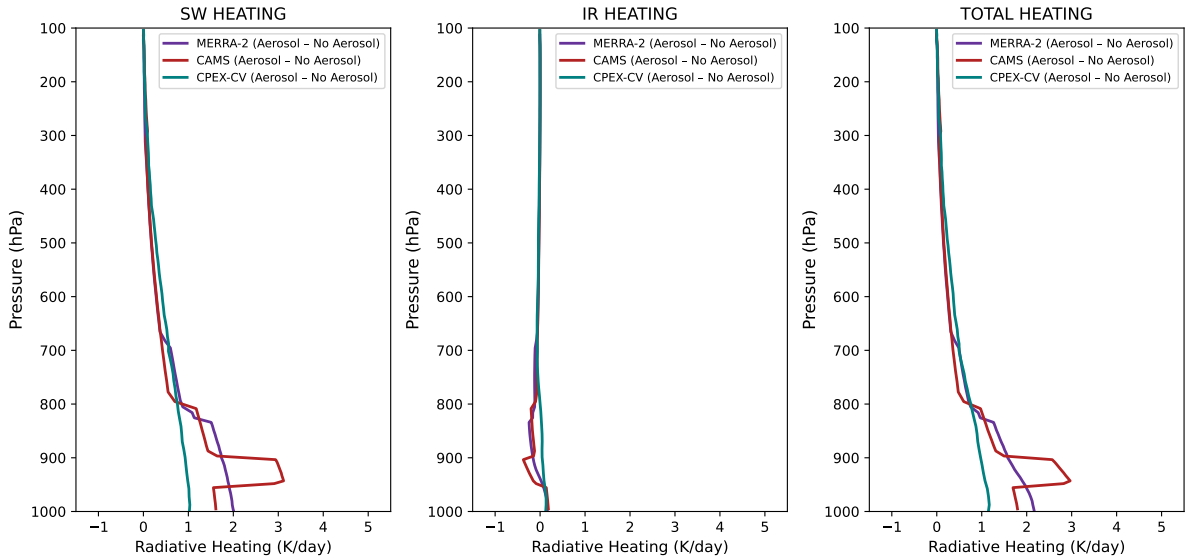

FIGURE 4.5: Heating rate difference between aerosol-aware and control run for MERRA-2 (purple), CAMS (red) and CPEX-CV (teal) on 09 September 2022. The left panel shows SW heating, the center panel shows LW/IR heating and the right panel shows total heating.

4.2.2 AEW 4 / Fiona

Figure 4.5 illustrates the difference in mean aerosol-induced heating rates during the research flight on 09 September 2022, where the average AOD value measured by CPEX-CV was 0.25. The strongest heating and the greatest difference between CPEX-CV and reanalysis datasets are seen in the SW heating profile. The CPEX-CV shows a SW heating of 1 K/day at the surface which decreases nearly linearly with height. This SW heating rate is greatly overestimated by both the MERRA-2 and CAMS reanalyses below 800 hPa, with a heating rate of 2 K/day at the surface for MERRA-2 and a heating rate of 1.6 K/day at the surface and reaching up to 3 K/day between 950 hPa and 900 hPa for CAMS. Differences in aerosol-induced LW/IR heating between CPEX-CV and reanalysis are minimal and mainly present between 950 hPa and 800 hPa.

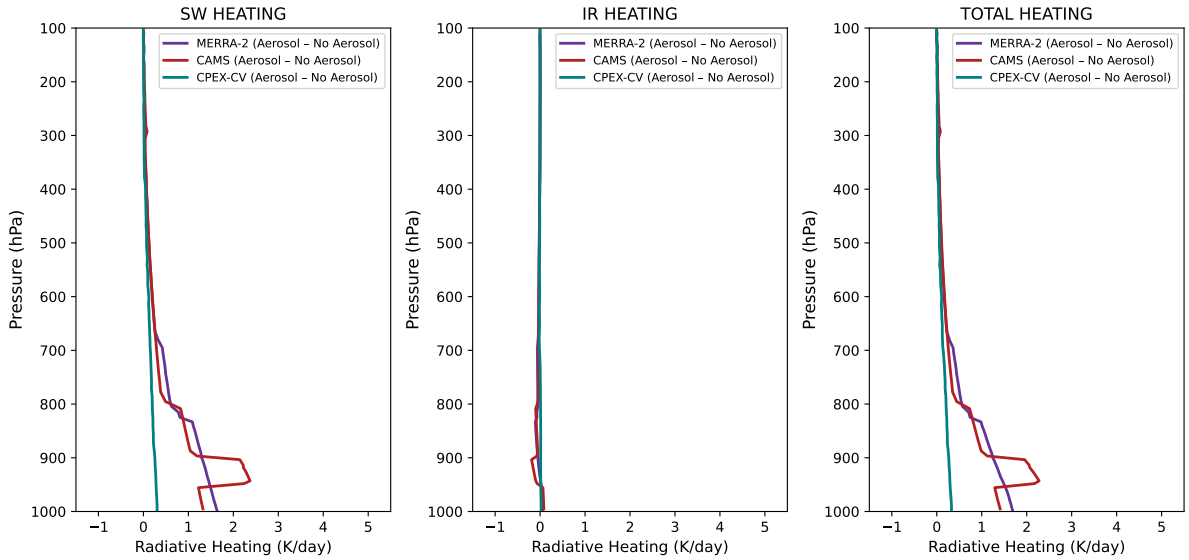

FIGURE 4.6: Heating rate difference between aerosol-aware and control run for MERRA-2 (purple), CAMS (red) and CPEX-CV (teal) on 14 September 2022. The left panel shows SW heating, the center panel shows LW/IR heating and the right panel shows total heating.

4.2.3 AEW 6 / Ian

Figure 4.5 illustrates the difference in mean aerosol-induced heating rates during the research flight on 14 September 2022, where the average AOD value measured by CPEX-CV was 0.06. The greatest difference between CPEX-CV and reanalysis datasets is once again seen in the SW heating profile, but the CPEX-CV aerosol-induced SW heating is much lower (0.3 K/day) than on 09 September 2022 (1 K/day) due to the lower AOD value. The SW heating rate is again strongly overestimated by both the MERRA-2 and CAMS reanalyses below 800 hPa, with a heating rate of 1.6 K/day at the surface for MERRA-2 and a heating rate of 1.2 K/day at the surface and reaching up to 2.4 K/day between 950 hPa and 900 hPa for CAMS. Because the AOD values are so low, differences in aerosol-induced LW/IR heating between CPEX-CV and reanalysis are close to zero.

4.2.4 AEW 8 / Hermine

Figure 4.7 shows striking differences in aerosol mean heating rates between the aerosol-aware and control run during the research flight on 22 September 2022, where the average AOD value measured by CPEX-CV was 1.02, over 4 times larger than on 09 September 2022. The CPEX-CV dataset shows a SW heating of 1.9 K/day at the surface, remaining between 1.9 K/day and 2.4 K/day up to 700 hPa, and decreasing with height above 800 hPa. This SW heating rate is once again overestimated by the MERRA-2 reanalysis below 800 hPa, with a heating rate of 2.3 K/day at the surface. The SW heating rate at the surface from CAMS is nearly identical to the heating rate from CPEX-CV, but the same increase in SW heating for CAMS between 950 hPa and 900 hPa attributed to the humidity profile as seen in previous cases reaches 4.4 K/day. Above 800 hPa, the two reanalyses greatly underestimate the SW heating rate in this case, with differences of over 1 K/day between CPEX-CV and reanalysis. The CPEX-CV data reveals that the heating is more evenly distributed throughout the column, whereas the reanalyses overestimate heating at the lower levels and underestimate heating at the upper levels.

4.2.5 Discussion

High dust concentration has the potential to strongly alter the heating profile, as illustrated in Figure 4.7, exacerbating differences between reanalysis and observation. In the context of developing AEWs, the heating rate differences between observation (CPEX-CV) and reanalysis represent a significant deficiency in atmospheric characterization,

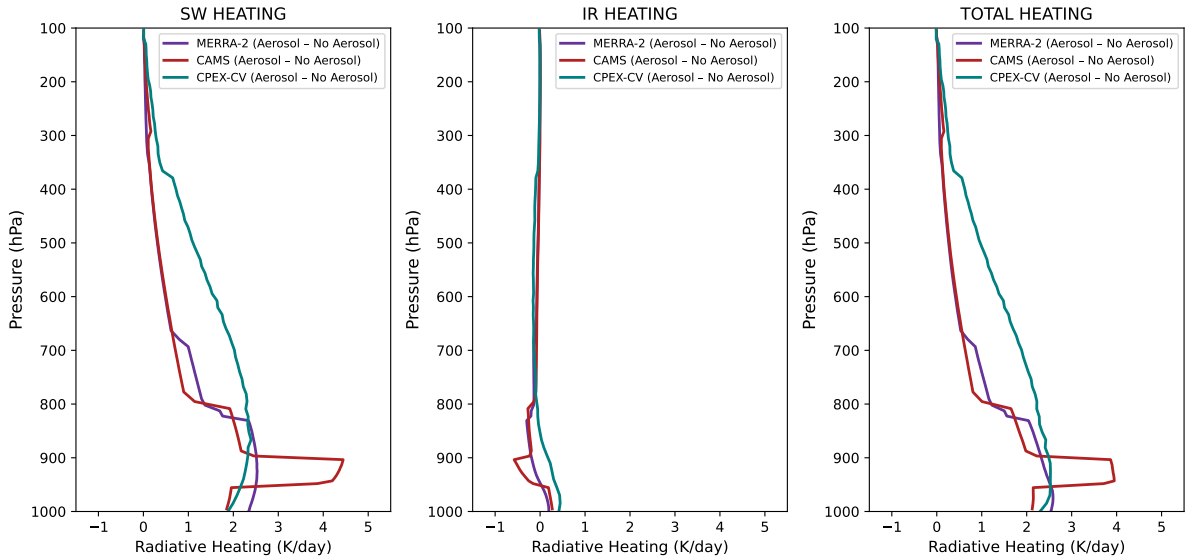

FIGURE 4.7: Heating rate difference between aerosol-aware and control run for MERRA-2 (purple), CAMS (red) and CPEX-CV (teal) on 22 September 2022. The left panel shows SW heating, the center panel shows LW/IR heating and the right panel shows total heating.

which must be addressed to avoid impacts on modeling outputs of such systems. Furthermore, Table 4.2 indicates the differences in AOD between CPEX-CV and reanalysis datasets are even greater at some locations, where CPEX-CV captured AOD values of up to 3.34 (as opposed to 2.49 and 1.30 for MERRA-2 and CAMS respectively), meaning that the differences captured in the mean heating rate profile in Figure 4.7 may be even larger at locations with higher AOD.

4.3 SW heating throughout the AEW development

4.3.1 Methodology

We analyze the structure of the dust-induced shortwave heating throughout the progression of Fiona, Ian and Hermine. We use the AEW tracker described in subsubsection 2.1.5.2 to collocate MERRA-2 and CAMS profiles with the center of the storm, and calculate dust-induced (aerosol-aware minus control) SW heating rates following the center of the storm as it progresses. As shown previously, the dust-induced total heating rates are driven primarily by SW radiation. Because there is no SW activity during nighttime only daytime profiles are studied. The profiles shown in Figure 4.8, Figure 4.9 and Figure 4.10 correspond to profiles at the closest gridpoint to the center of the storm as determined by the AEW tracker. The first profile corresponds to the first time-step where the center of the developing AEW was located over the ocean rather than land. The heating rate evolution is plotted from when the storm is intensifying over the Ocean to when it reaches land or begins to weaken. The last profile for Fiona corresponds to the last time-step before the storm made landfall over Puerto Rico, the last profiles for Ian corresponds to the last time step before it reached the Windward Islands, and the last profile for Hermine corresponds to the last time-step before the storm became a post-tropical remnant low.

4.3.2 Fiona

Figure 4.8 shows the vertical distribution of aerosol-induced SW heating throughout the evolution of the AEW leading to Hurricane Fiona. The heating rates are only shown during daytime, when SW heating is present. The strongest heating is concentrated between 1000 hPa and 800 hPa for the MERRA-2 dataset and varies between values of 0.52 K and 1.59 K/day throughout the progression of storm, with a first peak in heating on 12 September 2022 at 12:00 UTC caused by high dust loading in the Atlantic. The peak in heating on 18 September 2022 at 12:00 UTC is caused by high aerosol loading as the system approach the coast of Puerto Rico, with an anomalously high AOD value (0.64), while in previous time steps, AOD remained between 0.07 and 0.20. For the CAMS dataset, the heating peaks in the vertical around 900 hPa, as seen in previous figures, due to the differences in the humidity profile. The heating first peaks on 10 September 2022 at 12:00 UTC rather than on 12 September at 12:00 UTC as seen in the MERRA-2 dataset.

4.3.3 Ian

Similarly to Figure 4.8, Figure 4.9 shows the vertical distribution of aerosol-induced SW heating throughout the evolution of the AEW leading to Hurricane Ian. The structure of the heating resembles what is seen for Fiona, where the strongest heating is concentrated between 1000 hPa and 800 hPa for the MERRA-2 dataset. For both the MERRA-2 and CAMS reanalyses, the SW heating peaks at these levels on 17 September 2022 at 12:00 UTC, with a maximum heating rate of 1.26 K/day for MERRA-2 and a maximum

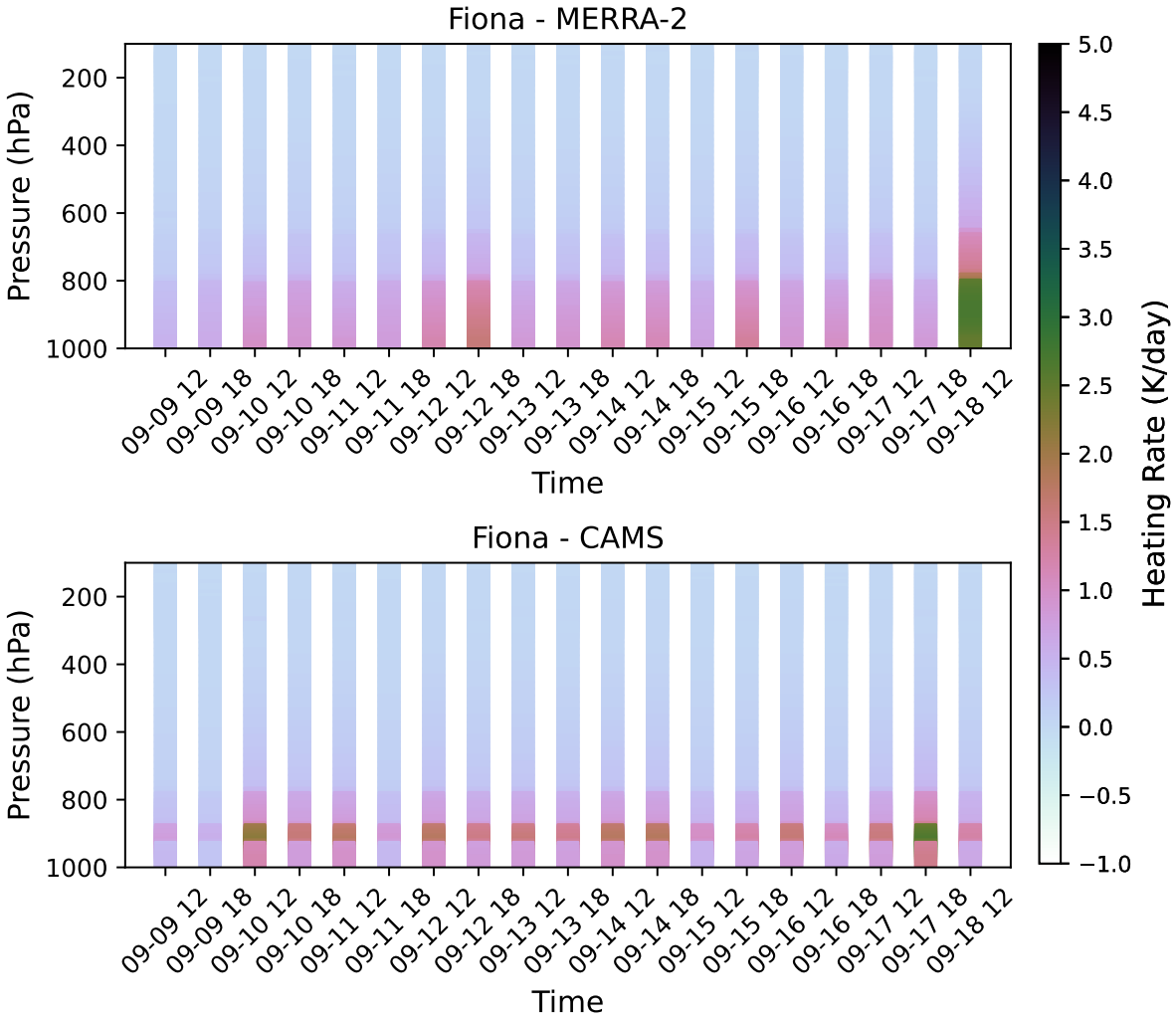

FIGURE 4.8: Vertical profiles of aerosol-induced SW heating rates (K/day) at the center of the AEW which developed into Hurricane Fiona for two reanalysis datasets (MERRA-2, top and CAMS, bottom).

heating rate of 2.54 K/day for CAMS. Once again, CAMS displays a strong peak in the vertical around 900 hPa. After the peak in heating, there is an overall decreasing trend in aerosol-induced shortwave heating as the storm progresses.

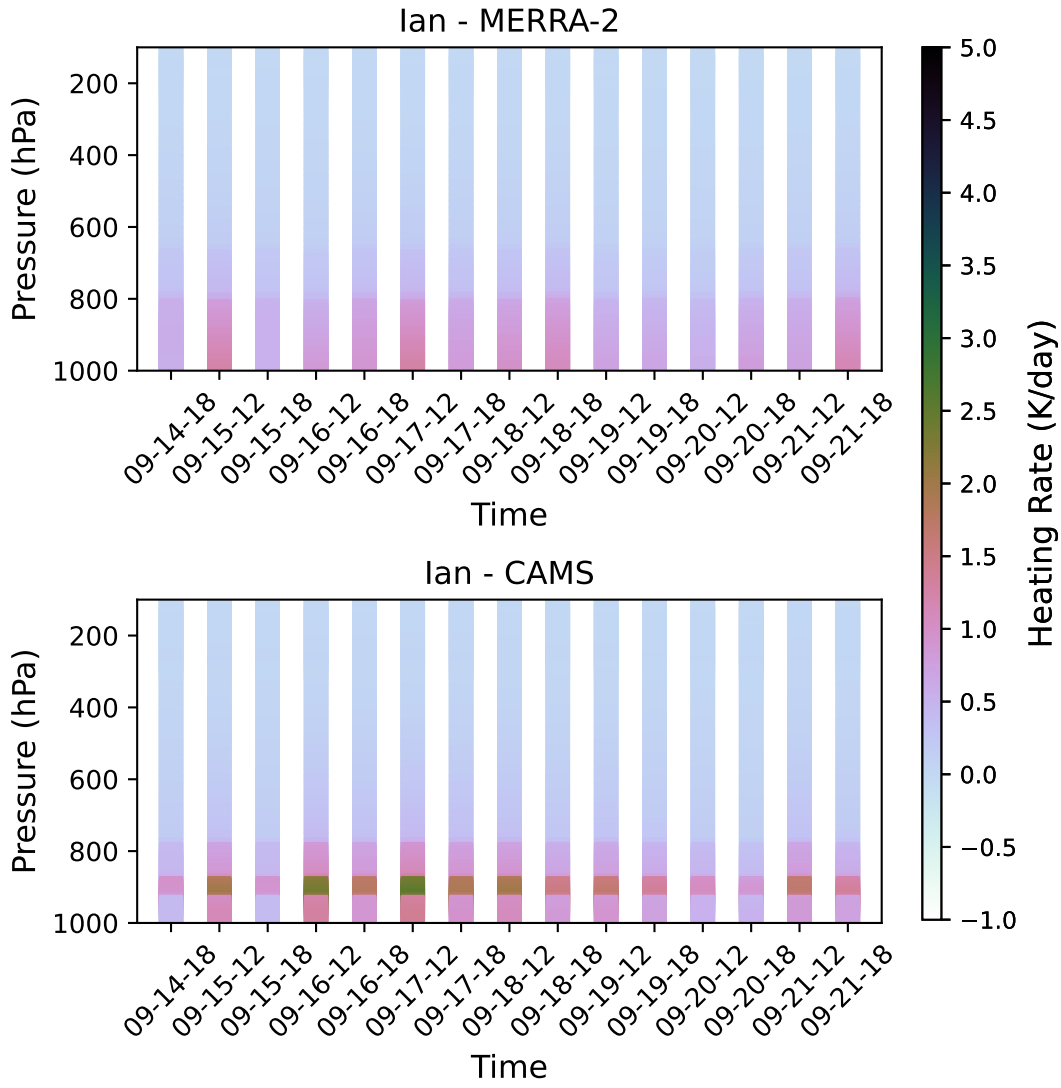

FIGURE 4.9: Vertical profiles of aerosol-induced SW heating rates (K/day) at the center of the AEW which developed into Hurricane Ian for two reanalysis datasets (MERRA-2, top and CAMS, bottom).

4.3.4 Hermine

Figure 4.10 shows that SW heating at 12 UTC on 23 September 2022 reaches 2.78 K/day according to MERRA-2. The CAMS profiles show similar results to the MERRA-2 dataset, but still overestimate the SW heating around 900 hPa, with a maximum heating value of 4.89 K/day. The peak heating at 12 UTC on 24 September 2022 is however lower

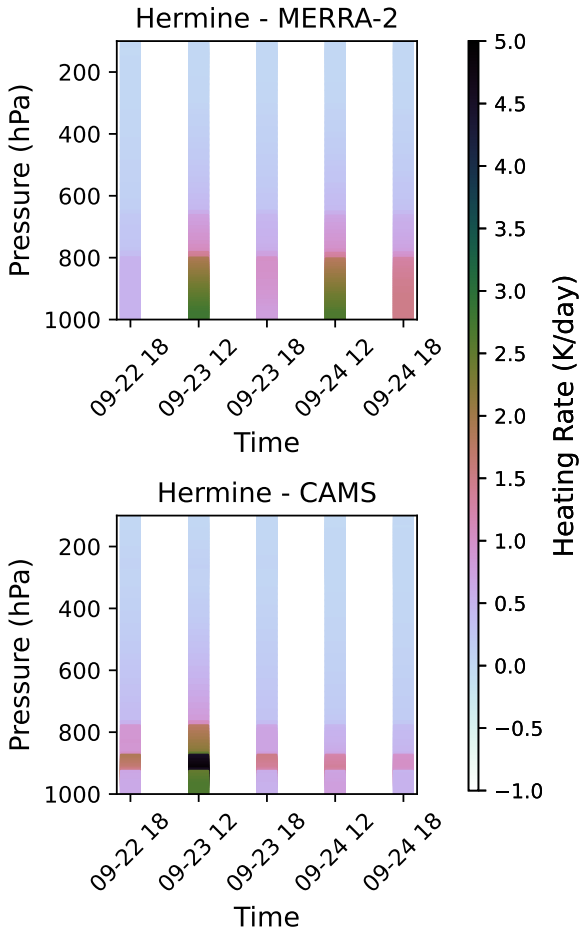

FIGURE 4.10: Vertical profiles of aerosol-induced SW heating rates (K/day) at the center of the AEW which developed into TS Hermine for two reanalysis datasets (MERRA-2, top and CAMS, bottom).

for CAMS with a peak heating value of 1.34 K/day versus 2.64 K/day for MERRA-2. Overall, the strong SW heating in this case is noteworthy in the context of the short lifespan of Hermine, which was unable to intensify to the scale of Fiona (Category 4 hurricane) or Ian (Category 5 hurricane). The maximum AOD value calculated by MERRA-2 at the center of the AEW for the profiles plotted during the development of Hermine was 0.4. However, as noted in previous sections, the CPEX-CV dataset measured values of AOD reaching up to 3.34 on 22 September 2022 in the environment of the developing AEW.

4.3.5 Discussion

Over the ocean, Sun and Zhao (2020) finds that dust tends to reduce specific humidity in the lower troposphere, particularly in regions with high aerosol loading, while simultaneously augmenting midlevel moisture levels. They also find that dust warms the lower troposphere, promoting convection and generating positive vorticity between approximately 800–1,000 hPa, where most of the aforementioned SW-induced heating rates in both reanalysis prevail. This warming effect can enhance vertical wind shear and consequently impacts environmental conditions in TC genesis regions. While we recognize this is not enough to draw a conclusion, since microphysics are not considered, and isolating the impact of thermodynamics to just aerosols is difficult, the large differences in heating at the lower levels of the atmosphere between the two cases raise the question of the impact of dust-induced radiative heating on AEW development.

Chapter 5

Summary and Conclusions

5.1 Summary

This study explores the impact of Saharan dust plumes on atmospheric heating rates in the context of African Easterly Wave (AEW) development using radiative transfer calculations based on reanalysis and airborne observations. It makes use of data from the Convective Processes Experiment – Cabo Verde (CPEX-CV) and two reanalysis datasets (MERRA-2 and CAMS). The study examined data from seven DC-8 flights during the CPEX-CV field campaign, with a special emphasis on three AEWs that developed into named tropical storms, two intensifying into hurricanes. The primary objectives include assessing the accuracy of reanalysis in depicting aerosol radiative properties, comparing the impact of Saharan dust on atmospheric heating rates in different AEW scenarios, and investigating the impact of observational data assimilation on model representation. The

methodology integrates observational data from CPEX-CV with a four-stream radiative transfer model (Fu-Liou-Gu RTM), utilizing aerosol profiles from MERRA-2 and CAMS reanalyses.

The research revealed notable differences in aerosol-induced heating rates between observational data (CPEX-CV) and reanalyses (MERRA-2 and CAMS). The reanalyses exhibited strong differences in extinction and atmospheric profiles compared to observed data, impacting the calculation of total heating rates. Both MERRA-2 and CAMS radiative transfer runs consistently overestimated shortwave (SW) heating rates below 800 hPa, with differences up to 2.05 K for the CAMS dataset in anomalous dust cases, and differences up to 0.6 K for MERRA-2 despite assimilating CPEX-CV data. These differences were driven by disparities in the representation of aerosol in extinction coefficient and AOD. MERRA-2 exhibited higher surface extinction coefficient than what was measured by CPEX-CV at the surface but failed to represent the variability throughout the tropospheric column that was captured by the observational data, revealing challenges in accurately representing aerosol effects in models. Differences in CAMS humidity and extinction profiles resulted in an overestimation of heating around 900 hPa. Both reanalyses also exhibited too high AOD values in background cases as contrasted with CPEX-CV data and too low values in the anomalous cases. A comparative analysis of an extreme dust event (June 2020 Godzilla dust storm) reinforced the findings, showcasing differences of over 5K in SW heating profiles between MERRA-2 and CAMS. This analysis provided further evidence of the robustness of observed profiles and the model's ability to capture aerosol-induced heating variations. Finally, a case study focusing on Hurricane Fiona,

Hurricane Ian and Tropical Storm Hermine illustrated the impact of aerosols on heating rates during specific research flights. Both reanalyses exhibited notable discrepancies in SW heating rates compared to observed data, with potential implications for forecasting the development of AEWs.

When considering the impact of heating rates on tropical cyclone development, a noteworthy observation emerges regarding varying dust concentrations and heating rates during different AEW events. The difference in aerosol-induced heating between flights with lower dust concentrations (mean AOD of 0.25 on 09 September and mean AOD of 0.06 on 14 September) and the flight with the highest dust concentrations (mean AOD = 1.02 on 22 September 2022) is on the order of 1 to 2 K/day, depending on the dataset. TS Hermine, which developed during the highest dust concentration day was a much shorter-lived storm and quickly weakened, as opposed to hurricanes Fiona and Ian which developed into major hurricanes. This raises the question of the role of dust induced heating in the development of these storms. Furthermore, the vertical structure of the heating was inaccurately represented by the reanalyses, specifically in the case of Hermine, where heating was overestimated below 800 hPa but underestimated above 800 hPa, the CPEX-CV dataset revealing a much more uniform heating distribution than the two reanalyses. Such errors in the heating profile are likely to impact the forecasting of the AEW development. This analysis only addresses one portion of a complex system, and a more comprehensive examination of environmental factors such as weather dynamics and dust and cloud microphysics is imperative for a comprehensive understanding of this problem. Recent studies using satellite data have also found that storms both remove

aerosol through precipitation scavenging as well as loft aerosol to higher levels, potentially influencing the vertical structure of aerosol heating in the atmosphere (Sauter and L'Ecuyer, 2017, Sauter et al., 2019). Despite these limitations, the observed patterns in this study underline the significance of incorporating dust-related variables in hurricane modeling studies.

5.2 Conclusions and Future Directions

This study emphasizes the importance of considering the vertical distribution and composition of aerosols in assessing their impact on AEWs. The research highlights the limitations of current reanalysis datasets in accurately capturing aerosol properties and their radiative effects, particularly at atmospheric levels critical for forecasting (1000-500 hPa). Despite the assimilation of observational data in the MERRA-2 reanalysis, substantial differences persist, indicating the need for further refinement in modeling aerosol distribution. Discrepancies in heating rates between reanalysis and airborne observations at key atmospheric levels, revealed by advanced radiative transfer modeling, have implications for weather forecasting. This points to the need for improved aerosol parameterizations in NWP models and provides an opportunity for refining our understanding of aerosol-AEW interactions in the Atlantic basin.

This study focused exclusively on aerosols and their impact on AEW development, without considering cloud-aerosol interactions. By isolating aerosol properties and their radiative impacts, the research provides a clearer understanding of how different types

and distributions of aerosols influence atmospheric heating rates and weather forecasting. This approach allows for more precise identification of discrepancies in reanalysis data and highlights the need for improved aerosol parameterizations in NWP models. However, incorporating cloud feedback is essential for a comprehensive understanding of atmospheric dynamics. Cloud interactions with aerosols can significantly alter radiative transfer and heating rates, impacting weather patterns and forecasting accuracy. Future studies should integrate cloud feedback mechanisms to fully capture the complexity of aerosol effects on AEW development and improve predictive models.

Moreover, future work on the impact of vertically resolved aerosols on atmospheric heating should explore the effects of various aerosol types globally, not just dust, by employing high-resolution models validated against observations. The tropical Atlantic AEW development region is also affected by biomass burning and tropospheric ozone enhancement, both of which could have significant implications for weather predictions and long-term climate projections. Integrating satellite-derived aerosol products with reanalysis data will improve aerosol representation, providing a more accurate depiction of their spatial and temporal distribution (Matus et al., 2019). Additionally, studying the broader impacts of aerosols on atmospheric dynamics, including cloud formation, precipitation patterns, and storm development, is necessary. A critical area to achieve these research needs is aerosol vertical profiling, which is currently lacking. Implementing detailed methods for vertical profiling will address this significant gap and provide deeper insights into aerosol behavior. To accomplish this, long-term observational campaigns across diverse regions or continuous spaceborne monitoring are needed. Currently, satellite profiling

of aerosol observations is very limited. Only NASA's CALIPSO mission could capture this variability, but this mission ended in 2022. Recently, the European Space Agency's EarthCARE satellite has been launched with similar aerosol vertical profiling capabilities via spaceborne lidar; however, like CALIPSO, its temporal coverage is limited to once every few weeks. Other satellite sensors capable of this type of measurement will not be launched until 2032 or later (National Academies of Sciences, Engineering, and Medicine, 2024).

Within the context of developing AEWs and subsequent storms, future observational campaigns should be enhanced with more frequent and extensive measurements. Real-time data assimilation and advanced tracking algorithms, potentially incorporating machine learning, could improve the accuracy of AEW position and intensity estimates. Additionally, detailed microphysical studies on aerosol composition, size distribution, and optical properties within AEWs are essential and could help refine similar studies to the one presented in this thesis.

Bibliography

Bauer, S. E. and S. Menon, 2012: Aerosol direct, indirect, semidirect, and surface albedo effects from sector contributions based on the ipcc ar5 emissions for preindustrial and present-day conditions. *Journal of Geophysical Research: Atmospheres*, **117**.

Bedka, K. M., A. R. Nehrir, M. Kavaya, R. Barton-Grimley, M. Beaubien, B. Carroll, J. Collins, J. Cooney, G. D. Emmitt, S. Greco, S. Kooi, T. Lee, Z. Liu, S. Rodier, and G. Skofronick-Jackson, 2021: Airborne lidar observations of wind, water vapor, and aerosol profiles during the nasa aeolus calibration and validation (cal/val) test flight campaign. *Atmospheric Measurement Techniques*, **14**, 4305–4334, doi:10.5194/amt-14-4305-2021.

URL `https://amt.copernicus.org/articles/14/4305/2021/`

Bercos-Hickey, E., T. R. Nathan, and S.-H. Chen, 2017: Saharan dust and the african easterly jet–african easterly wave system: Structure, location and energetics. *Quarterly Journal of the Royal Meteorological Society*, **143**, 2797–2808.

Buchard, V., C. Randles, A. Da Silva, A. Darmenov, P. Colarco, R. Govindaraju, R. Ferrare, J. Hair, A. Beyersdorf, L. Ziemba, et al., 2017: The merra-2 aerosol reanalysis,

1980 onward. part ii: Evaluation and case studies. *Journal of Climate*, **30**, 6851–6872.

Burpee, R. W., 1972: The origin and structure of easterly waves in the lower troposphere of north africa. *Journal of the Atmospheric Sciences*, **29**, 77–90.

Carlson, T. N., 1979: Atmospheric turbidity in saharan dust outbreaks as determined by analyses of satellite brightness data. *Monthly Weather Review*, **107**, 322–335.

Carlson, T. N. and S. G. Benjamin, 1980: Radiative heating rates for saharan dust. *Journal of the Atmospheric Sciences*, **37**, 193–213.

Carroll, B. J., A. R. Nehrir, S. A. Kooi, J. E. Collins, R. A. Barton-Grimley, A. Notari, D. B. Harper, and J. Lee, 2022: Differential absorption lidar measurements of water vapor by the high altitude lidar observatory (halo): retrieval framework and first results. *Atmospheric Measurement Techniques*, **15**, 605–626.

Charney, J. G. and M. E. Stern, 1962: On the stability of internal baroclinic jets in a rotating atmosphere. *Journal of the Atmospheric Sciences*, **19**, 159–172.

Dubovik, O., B. Holben, T. F. Eck, A. Smirnov, Y. J. Kaufman, M. D. King, D. Tanré, and I. Slutsker, 2002: Variability of absorption and optical properties of key aerosol types observed in worldwide locations. *Journal of the atmospheric sciences*, **59**, 590–608.

Dunion, J. P. and C. S. Velden, 2004: The impact of the saharan air layer on atlantic tropical cyclone activity. *Bulletin of the American Meteorological Society*, **85**, 353–366.

Eck, T. F., B. Holben, J. Reid, O. Dubovik, A. Smirnov, N. O'neill, I. Slutsker, and S. Kinne, 1999: Wavelength dependence of the optical depth of biomass burning, urban, and desert dust aerosols. *Journal of Geophysical Research: Atmospheres*, **104**, 31333–31349.

Fu, Q. and K. Liou, 1992: On the correlated k-distribution method for radiative transfer in nonhomogeneous atmospheres. *Journal of Atmospheric Sciences*, **49**, 2139–2156.

Fu, Q., K. Liou, M. Cribb, T. Charlock, and A. Grossman, 1997: Multiple scattering parameterization in thermal infrared radiative transfer. *Journal of the atmospheric sciences*, **54**, 2799–2812.

Fu, Q. and K. N. Liou, 1993: Parameterization of the radiative properties of cirrus clouds. *Journal of Atmospheric Sciences*, **50**, 2008–2025.

Gelaro, R., W. McCarty, M. J. Suárez, R. Todling, A. Molod, L. Takacs, C. A. Randles, A. Darmenov, M. G. Bosilovich, R. Reichle, et al., 2017: The modern-era retrospective analysis for research and applications, version 2 (merra-2). *Journal of climate*, **30**, 5419–5454.

GMAO, 2023: Supplemental documentation for geos aerosol products. Technical report, NASA GMAO.

Grogan, D. F., T. R. Nathan, and S.-H. Chen, 2016: Effects of saharan dust on the linear dynamics of african easterly waves. *Journal of the Atmospheric Sciences*, **73**, 891–911.

— 2017: Saharan dust and the nonlinear evolution of the african easterly jet–african easterly wave system. *Journal of the Atmospheric Sciences*, **74**, 27–47.

— 2019: Structural changes in the african easterly jet and its role in mediating the effects of saharan dust on the linear dynamics of african easterly waves. *Journal of the Atmospheric Sciences*, **76**, 3351–3365.

Grogan, D. F. and C. D. Thorncroft, 2019: The characteristics of african easterly waves coupled to saharan mineral dust aerosols. *Quarterly Journal of the Royal Meteorological Society*, **145**, 1130–1146.

Grogan, D. F. P., C.-H. Lu, S.-W. Wei, and S.-P. Chen, 2022: Investigating the impact of saharan dust aerosols on analyses and forecasts of african easterly waves by constraining aerosol effects in radiance data assimilation. *Atmospheric Chemistry and Physics*, **22**, 2385–2398.

Gu, Y., K. Liou, S. Ou, and R. Fovell, 2011: Cirrus cloud simulations using wrf with improved radiation parameterization and increased vertical resolution. *Journal of Geophysical Research: Atmospheres*, **116**.

Hess, M., P. Koepke, and I. Schult, 1998: Optical properties of aerosols and clouds: The software package opac. *Bulletin of the American meteorological society*, **79**, 831–844.

Hock, F. J. L., T. F., 1999: The ncar gps dropwindsonde. *Bull. Amer. Meteor. Soc., 80, 407-420*, **80**, 407–420.

Huang, J., C. Zhang, and J. M. Prospero, 2010: African dust outbreaks: A satellite perspective of temporal and spatial variability over the tropical atlantic ocean. *Journal of Geophysical Research: Atmospheres*, **115**.

Huffman, G. J., D. T. Bolvin, D. Braithwaite, K.-L. Hsu, R. J. Joyce, C. Kidd, E. J. Nelkin, S. Sorooshian, E. F. Stocker, J. Tan, et al., 2020: Integrated multi-satellite retrievals for the global precipitation measurement (gpm) mission (imerg). *Satellite Precipitation Measurement: Volume 1*, 343–353.

Inness, A., M. Ades, A. Agustí-Panareda, J. Barré, A. Benedictow, A.-M. Blechschmidt, J. J. Dominguez, R. Engelen, H. Eskes, J. Flemming, et al., 2019: The cams reanalysis of atmospheric composition. *Atmospheric Chemistry and Physics*, **19**, 3515–3556.

Ismail, S., R. A. Ferrare, E. V. Browell, G. Chen, B. Anderson, S. A. Kooi, A. Notari, C. F. Butler, S. Burton, M. Fenn, et al., 2010: Lase measurements of water vapor, aerosol, and cloud distributions in saharan air layers and tropical disturbances. *Journal of the atmospheric sciences*, **67**, 1026–1047.

Jones, C., N. Mahowald, and C. Luo, 2004: Observational evidence of african desert dust intensification of easterly waves. *Geophysical research letters*, **31**.

Jury, M. R. and M. J. Santiago, 2010: Composite analysis of dust impacts on african easterly waves in the moderate resolution imaging spectrometer era. *Journal of Geophysical Research: Atmospheres*, **115**.

Karyampudi, V. M., S. P. Palm, J. A. Reagen, H. Fang, W. B. Grant, R. M. Hoff, C. Moulin, H. F. Pierce, O. Torres, E. V. Browell, et al., 1999: Validation of the saharan dust plume conceptual model using lidar, meteosat, and ecmwf data. *Bulletin of the American Meteorological Society*, **80**, 1045–1076.

Landsea, C. W., 1993: A climatology of intense (or major) atlantic hurricanes. *Monthly weather review*, **121**, 1703–1713.

Lavaysse, C., J.-P. Chaboureau, and C. Flamant, 2011: Dust impact on the west african heat low in summertime. *Quarterly Journal of the Royal Meteorological Society*, **137**, 1227–1240.

Lawton, Q. A., S. J. Majumdar, K. Dotterer, C. Thorncroft, and C. J. Schreck III, 2022: The influence of convectively coupled kelvin waves on african easterly waves in a wave-following framework. *Monthly weather review*, **150**, 2055–2072.

Lei, L., T. A. Berkoff, G. Gronoff, J. Su, A. R. Nehrir, Y. Wu, F. Moshary, and S. Kuang, 2022: Retrieval of uvb aerosol extinction profiles from the ground-based langley mobile ozone lidar (lmol) system. *Atmospheric Measurement Techniques*, **15**, 2465–2478.

Lenhardt, E. D., L. Gao, J. Redemann, F. Xu, S. P. Burton, B. Cairns, I. Chang, R. A. Ferrare, C. A. Hostetler, P. E. Saide, et al., 2022: Use of lidar aerosol extinction and backscatter coefficients to estimate cloud condensation nuclei (ccn) concentrations in the southeast atlantic. *Atmospheric Measurement Techniques Discussions*, **2022**, 1–30.

Linke, C., O. Möhler, A. Veres, Á. Mohácsi, Z. Bozóki, G. Szabó, and M. Schnaiter, 2006: Optical properties and mineralogical composition of different saharan mineral dust samples: a laboratory study. *Atmospheric Chemistry and Physics*, **6**, 3315–3323.

Liou, K.-N., Q. Fu, and T. P. Ackerman, 1988: A simple formulation of the delta-four-stream approximation for radiative transfer parameterizations. *Journal of Atmospheric Sciences*, **45**, 1940–1948.

Ma, P.-L., K. Zhang, J. J. Shi, T. Matsui, and A. Arking, 2012: Direct radiative effect of mineral dust on the development of african easterly waves in late summer, 2003–07. *Journal of applied meteorology and climatology*, **51**, 2090–2104.

Matus, A. V., T. S. L'Ecuyer, and D. S. Henderson, 2019: New estimates of aerosol direct radiative effects and forcing from a-train satellite observations. *Geophysical Research Letters*, **46**, 8338–8346.

Mulcahy, J., D. Walters, N. Bellouin, and S. Milton, 2014: Impacts of increasing the aerosol complexity in the met office global numerical weather prediction model. *Atmospheric Chemistry and Physics*, **14**, 4749–4778.

Nalli, N. R., E. Joseph, V. R. Morris, C. D. Barnet, W. W. Wolf, D. Wolfe, P. J. Minnett, M. Szczodrak, M. A. Izaguirre, R. Lumpkin, et al., 2011: Multiyear observations of the tropical atlantic atmosphere: Multidisciplinary applications of the noaa aerosols and ocean science expeditions. *Bulletin of the American Meteorological Society*, **92**, 765–789.

Nathan, T. R., D. F. Grogan, and S.-H. Chen, 2017: Subcritical destabilization of african easterly waves by saharan mineral dust. *Journal of the Atmospheric Sciences*, **74**, 1039–1055.

National Academies of Sciences, Engineering, and Medicine, 2024: *Thriving on Our Changing Planet: A Midterm Assessment of Progress Toward Implementation of the Decadal Survey*. The National Academies Press, Washington, DC.

URL https://doi.org/10.17226/27743

National Hurricane Center, 2022a: Hurricane dorian (al092022): 23 september - 30 september 2022. Retrieved from the National Hurricane Center website.

URL https://www.nhc.noaa.gov/data/tcr/AL092022_Ian.pdf

— 2022b: Hurricane dorian (al102022): 23 september - 24 september 2022. Retrieved from the National Hurricane Center website.

URL https://www.nhc.noaa.gov/data/tcr/AL102022_Hermine.pdf

— 2022c: Hurricane fiona (al072022): 14 september - 23 september 2022. Retrieved from the National Hurricane Center website.

URL https://www.nhc.noaa.gov/data/tcr/AL072022_Fiona.pdf

Norquist, D. C., E. E. Recker, and R. J. Reed, 1977: The energetics of african wave disturbances as observed during phase iii of gate. *Monthly Weather Review*, **105**, 334–342.

Nowottnick, E. P., A. K. Rowe, A. R. Nehrir, J. A. Zawislak, A. J. Piña, W. McCarty, R. A. Barton-Grimley, K. M. Bedka, J. R. Bennett, A. Brammer, M. E. Buzanowicz, G. Chen, S.-H. Chen, S. S. Chen, P. R. Colarco, J. W. Cooney, E. Crosbie, J. Doyle, T. Fehr, R. A. Ferrare, S. D. Harrah, S. M. Hristova-Veleva, B. H. Lambrigtsen, Q. A. Lawton, A. Lee, E. Marinou, E. R. Martin, G. Močnik, E. Mazza, R. Rodriguez Monje, K. M. Núñez Ocasio, Z. Pu, M. Rajagopal, J. S. Reid, C. E. Robinson, R. Rios-Berrios, B. D. Rodenkirch, N. Sakaeda, V. Salazar, M. A. Shook, L. Sinclair, G. M. Skofronick-Jackson, K. L. Thornhill, R. D. Torn, D. P. Van Gilst, P. G. Veals, H. Vömel, S. Wong, S.-N. Wu, L. D. Ziemba, and E. J. Zipser, 2024: Dust, convection, winds, and waves: The 2022 nasa cpex-cv campaign. *Bull. Amer. Meteor. Soc.*, in revision.

Nowottnick, E. P., J. Zawislak, A. R. Nehrir, H. Maring, A. J. Piña, W. McCarty, J. S. Reid, S.-H. Chen, A. K. Rowe, N. Sakaeda, et al., 2023: The nasa convective processes experiment-cabo verde (cpex-cv): Mission overview and saharan dust measurements obtained in the east atlantic in september 2022. *103rd AMS Annual Meeting*, AMS.

Oyola, M. I., 2015: *Implementation of a Global Dust Physical Sea Surface Temperature Retrieval For Numerical Weather Prediction Applications*. Ph.D. thesis, Howard University.

Oyola, M. I., J. R. Campbell, P. Xian, A. Bucholtz, R. A. Ferrare, S. P. Burton, O. Kalashnikova, B. C. Ruston, and S. Lolli, 2019: Quantifying the direct radiative effect of absorbing aerosols for numerical weather prediction: a case study. *Atmospheric Chemistry and Physics*, **19**, 205–218, doi:10.5194/acp-19-205-2019.

URL https://acp.copernicus.org/articles/19/205/2019/

Petty, G. W., 2008: *A First Course in Atmospheric Thermodynamics.*. Sundog Publishing, 337 pp.

Pratt, A. S. and J. L. Evans, 2009: Potential impacts of the saharan air layer on numerical model forecasts of north atlantic tropical cyclogenesis. *Weather and forecasting*, **24**, 420–435.

Prospero, J., R. Charlson, V. Mohnen, R. Jaenicke, A. Delany, J. Moyers, W. Zoller, and K. Rahn, 1983: The atmospheric aerosol system: An overview. *Reviews of Geophysics*, **21**, 1607–1629.

Pytharoulis, I. and C. Thorncroft, 1999: The low-level structure of african easterly waves in 1995. *Monthly Weather Review*, **127**, 2266–2280.

Quijano, A. L., I. N. Sokolik, and O. B. Toon, 2000: Radiative heating rates and direct radiative forcing by mineral dust in cloudy atmospheric conditions. *Journal of Geophysical Research: Atmospheres*, **105**, 12207–12219.

Ramanathan, V., P. J. Crutzen, J. Kiehl, and D. Rosenfeld, 2001: Aerosols, climate, and the hydrological cycle. *science*, **294**, 2119–2124.

Randles, C., A. Da Silva, V. Buchard, P. Colarco, A. Darmenov, R. Govindaraju, A. Smirnov, B. Holben, R. Ferrare, J. Hair, et al., 2017: The merra-2 aerosol reanalysis, 1980 onward. part i: System description and data assimilation evaluation. *Journal of climate*, **30**, 6823–6850.

Reale, O., W. K. Lau, K.-M. Kim, and E. Brin, 2009: Atlantic tropical cyclogenetic processes during sop-3 namma in the geos-5 global data assimilation and forecast system. *Journal of the atmospheric sciences*, **66**, 3563–3578.

Sauter, K. and T. S. L'Ecuyer, 2017: Observational evidence for the vertical redistribution and scavenging of saharan dust by tropical cyclones. *Geophysical Research Letters*, **44**, 6421–6430.

Sauter, K., T. S. L'Ecuyer, S. C. van den Heever, C. Twohy, A. Heidinger, S. Wanzong, and N. Wood, 2019: The observed influence of tropical convection on the saharan dust layer. *Journal of Geophysical Research: Atmospheres*, **124**, 10896–10912.

Sun, Y. and C. Zhao, 2020: Influence of saharan dust on the large-scale meteorological environment for development of tropical cyclone over north atlantic ocean basin. *Journal of Geophysical Research: Atmospheres*, **125**, e2020JD033454.

Swap, R., S. Ulanski, M. Cobbett, and M. Garstang, 1996: Temporal and spatial characteristics of saharan dust outbreaks. *Journal of Geophysical Research: Atmospheres*, **101**, 4205–4220.

Takemura, T., T. Nakajima, O. Dubovik, B. N. Holben, and S. Kinne, 2002: Single-scattering albedo and radiative forcing of various aerosol species with a global three-dimensional model. *Journal of Climate*, **15**, 333–352.

Thorncroft, C. D., N. M. Hall, and G. N. Kiladis, 2008: Three-dimensional structure and dynamics of african easterly waves. part iii: Genesis. *Journal of the Atmospheric Sciences*, **65**, 3596–3607.

Toll, V., E. Gleeson, K. Nielsen, A. Männik, J. Mašek, L. Rontu, and P. Post, 2016: Impacts of the direct radiative effect of aerosols in numerical weather prediction over europe using the aladin-hirlam nwp system. *Atmospheric Research*, **172**, 163–173.

Winker, D. M., M. A. Vaughan, A. Omar, Y. Hu, K. A. Powell, Z. Liu, W. H. Hunt, and S. A. Young, 2009: Overview of the calipso mission and caliop data processing algorithms. *Journal of Atmospheric and Oceanic Technology*, **26**, 2310–2323.

Yu, H., Q. Tan, L. Zhou, Y. Zhou, H. Bian, M. Chin, C. L. Ryder, R. C. Levy, Y. Pradhan, Y. Shi, et al., 2021: Observation and modeling of the historic "godzilla" african dust intrusion into the caribbean basin and the southern us in june 2020. *Atmospheric Chemistry and Physics*, **21**, 12359–12383.

Zhang, J., J. S. Reid, M. Christensen, and A. Benedetti, 2016: An evaluation of the impact of aerosol particles on weather forecasts from a biomass burning aerosol event over the midwestern united states: observational-based analysis of surface temperature. *Atmospheric Chemistry and Physics*, **16**, 6475–6494.

Zipser, E. J., C. H. Twohy, S.-C. Tsay, K. L. Thornhill, S. Tanelli, R. Ross, T. Krishnamurti, Q. Ji, G. Jenkins, S. Ismail, et al., 2009: The saharan air layer and the fate of african easterly waves—nasa's amma field study of tropical cyclogenesis. *Bulletin of the American Meteorological Society*, **90**, 1137–1156.